NASA TECHNICAL MEMORANDUM

NASA-TM- 75811

79N33123

X-RAY OPTICAL PROPERTIES OF A WOLTER TELESCOPE

A. Ondrusch

Translation of "Röntgenoptische Eigenschaften Eines Wolterteleskops", Max-Planck-Institut fuer Physik und Astrophysik, Institut fur Extraterrestrische Physik, Garching, West Germany, RPT MPI-PAE/EXTRATERR-146, Sept. 1978, 92 pages

NATIONAL AERONAUTICS AND SPACE ADMINISTRATION
WASHINGTON, D.C. 20546, FEBRUARY, 1980

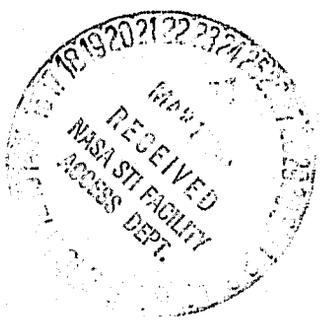

STANDARD TITLE PAGE

1. Report No. NASA TM - 75811	2. Government Accession No.	3. Recipient's Catalog No.
4. Title and Subtitle X-RAY OPTICAL PROPERTIES OF A WOLTER TELESCOPE		5. Report Date 6. Performing Organization Code
7. Author(s) A. Ondrusch		8. Performing Organization Report No. 10. Work Unit No.
9. Performing Organization Name and Address Leo Kanner and Assoc. P.O. Box 5187 Redwood City, Calif. 94063		11. Contract or Grant No. NASw-3199 13. Type of Report and Period Covered Translation
12. Sponsoring Agency Name and Address National Aeronautics and Space Administration Washington, D. C. 20546		14. Sponsoring Agency Code

15. Supplementary Notes

Translation of "Rontgenoptische Eigenschaften Eines Wolterteleskops", Max-Planck-Institut fuer Physik und Astrophysik, Institut fur Extraterrestrische Physik, Garching, West Germany, RPT MPI-PAE/EXTRATERR-146, Sept. 1978, 92 pages (N79-33123)

16. Abstract

Physical properties and fabrication sequence of Wolter telescope made by C. Zeiss Co. under contract to the MPE are discussed. Such telescopes are intended to examine the dust scattering halos after being placed in orbit by a booster rocket launched from Australia.

17. Key Words (Selected by Author(s))	18. Distribution Statement
	Unclassified unlimited

19. Security Classif. (of this report)	20. Security Classif. (of this page)	21. No. of Pages	22. Price
Unclassified	Unclassified	77	

NASA-HQ

X-RAY OPTICAL PROPERTIES OF A WOLTER TELESCOPE

A. Ondrusch

1. Introduction

/2*

Probably one of the strongest driving forces in man is the dissatisfaction with present levels of achievement and the never-ending thirst for knowledge. These two drives have brought x-ray astronomy within 30 years to a level comparable with that of optic astronomy at the time of Galileo. Just as he held his first telescope in his hands at that time, today the first useful imaging systems in the x-ray spheres are available.

Development work began at the institute with the construction of the rocket payload "ASTRO-8" consisting of 12 parabolic mirrors with proportional counters as focal instruments. The next step was the construction of three Wolter Type I telescopes with a maximum diameter of 32 cm which were manufactured--like the ASTRO-8--by C. Zeiss Company, Oberkochen.

The principle of the Type I telescrope was first suggested by H. Wolter 1952 (5). It consists of a rotation paraboloid and a coaxial and cofocal rotation hyperboloid which are illuminated under oblique incidence. The great advantage of such telescopes is the enormous efficiency and high image contrast with relatively high resolution (5.9 arcsec FWHM for the 32 cm telescope) with the potential for using spectroscopy. After the sun was observed for the first time in 1949 from V2-rockets in x-ray light, in 1962 the first extra-solar source Sco X-1 was discovered. Subsequently, the search for other extra-solar sources began with the UHURU satellites and the yield was so great in spite of the rather mediocre means available (in comparison to today) that an extensive catalog was prepared. With HEAO-1 in 1977, another satellite was launched to perform measurements in the energy range from 0.15 KeV to 20 MeV. It did not contain any imaging optics, but with its collimiter proportional counter of 8800 cm^2 sensitive surface area in the region of weak x-ray radiation, it is already much more sensitive then UHURU. Today about 200 x-ray sources are known, some of which can also be identified with optic lenses. But much is still unclear. For instance, there are whole series of x-ray sources which cannot yet be identified with objects known from other spectral ranges. For a part of the known x-ray sources, today we know rather certainly which type of star it is but it is not known, for instance for Cyg X-3, whether it is an old or a young neutron star. Likewise we know very little about the structures of known sources. Better measurement data are expected from HEAO-B, a 4x stacked Wolter Type I telescope launched on 11/17 of this year. It is probably the most powerful x-ray telescope in the world having a collector surface

---

*Numbers in the margin indicate pagination in the foreign text.

/3

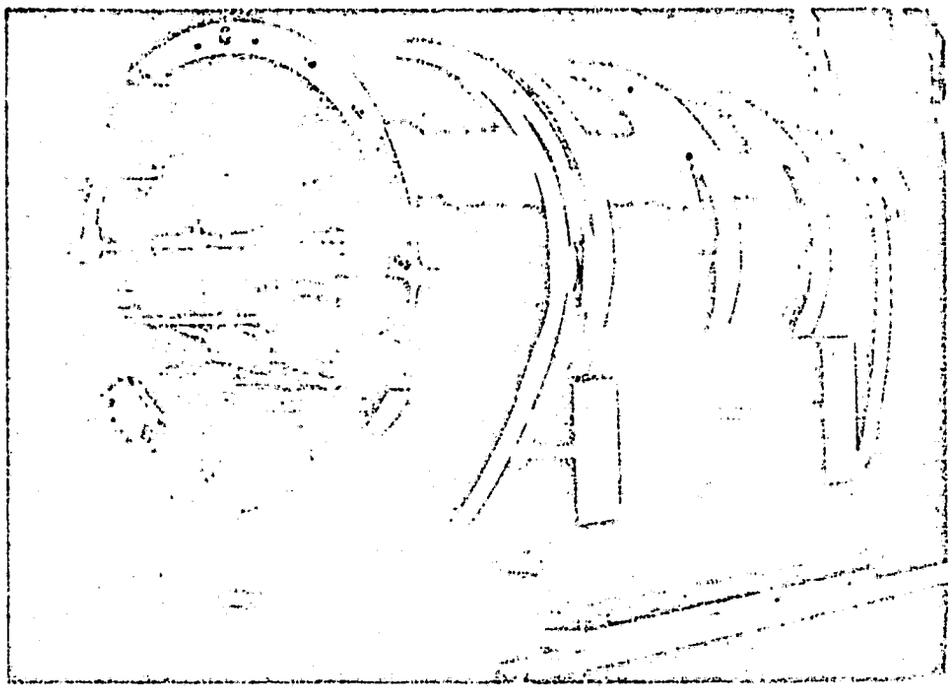

The 32 cm-Wolter Type I Telescope

area of about 200 cm^2 at 0.93 KeV. If we were to perform an all-sky survey with this telescope, we could probably discover several 10,000 new x-ray sources because of the 10^4 times greater sensitivity than UHURU. HEAO-B will observe only about 3% of the sky looking primarily at known sources and studying their structures. /4

The quality of such a telescope is determined primarily by two factors:

1. The width of a point image of an infinitely distant source (FWHM).

2. The height and width of the distribution caused by scattering of x-ray radiation from the surface of the mirror.

With this type of telescope, 3rd and higher order imaging errors and manufacture-induced flaws occur; these latter flaws generally predominate over the former. There are two particularly disturbing factors:

1. The so-called "microroughness" which always remains even on highly polished surfaces and which leads to scattering x-ray radiation. Whereas for optic wavelengths of such mirrors the Rayleigh criterion $\sqrt{g} = \frac{4\pi \sin\alpha}{\lambda} \ll 1$ is fulfilled, the expression for $\lambda = 10\text{Å}$ and an angle of incidence of 1° is equal to one. Therefore the scattering cannot be neglected and is discussed in this paper with the Beckmann theory. For the integral scattering fraction this provides the expression $S = 1 - e^{-g}$ with $g = 2k\sin\alpha \cdot \sigma$, whereby σ is the average quadratic deviation

from the mirror plane. Figures 1 and 2 illustrate this. We will later see that the scattering halo can be approximated by a declining e-function.

In addition, in this report the imaging error, the influence of diffraction, the temperature, non-paraxial incidence and divergent illumination shall be studied. The results are compared with measurements both in the optic and in the x-ray range; x-ray wavelengths will also be compared with measurements taken by the individual mirror segments. /5

With the 32 cm telescope scattering halos shall be studied primarily. These are caused by small angle scattering of the radiation emitted from the x-ray stars by interstellar dust. From this results the requirement to build a telescope with the smallest possible scattering. But the structures of pronounced x-ray sources and supernova remnants shall also be studied. Such remnants are the Crab nebula, the Cygnus loop and Puppis A, with the accurate observation program directed toward the approximate 300 second long measurement time after the exact starting schedule.

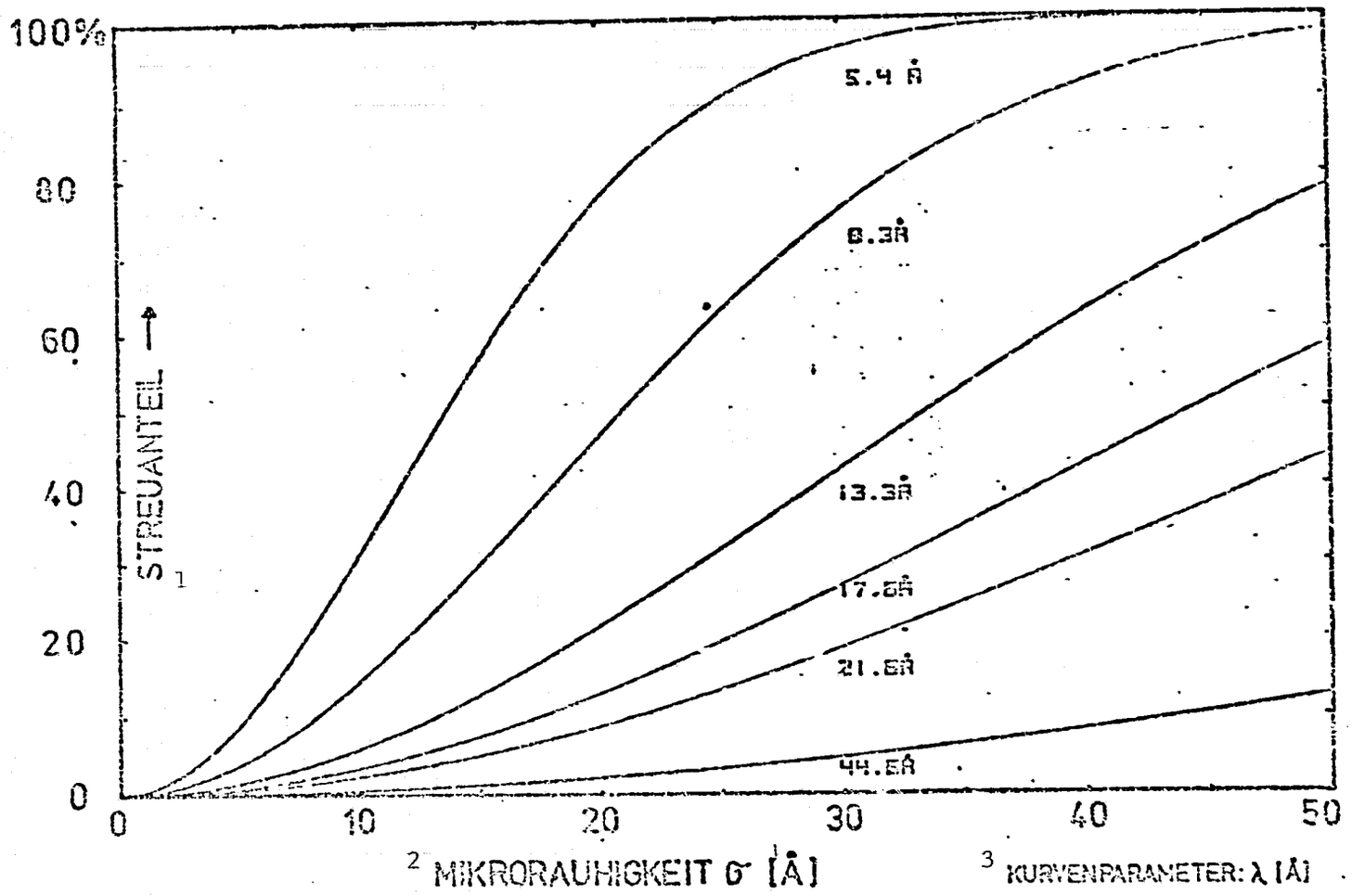

Figure 1: Dependence of the integral scattering fraction on microroughness for an angle of incidence of 1.5° (Curve parameter: λ [Å] for simple reflextion)

Key: 1-Scattering angle 2-microroughness 3-curve parameter

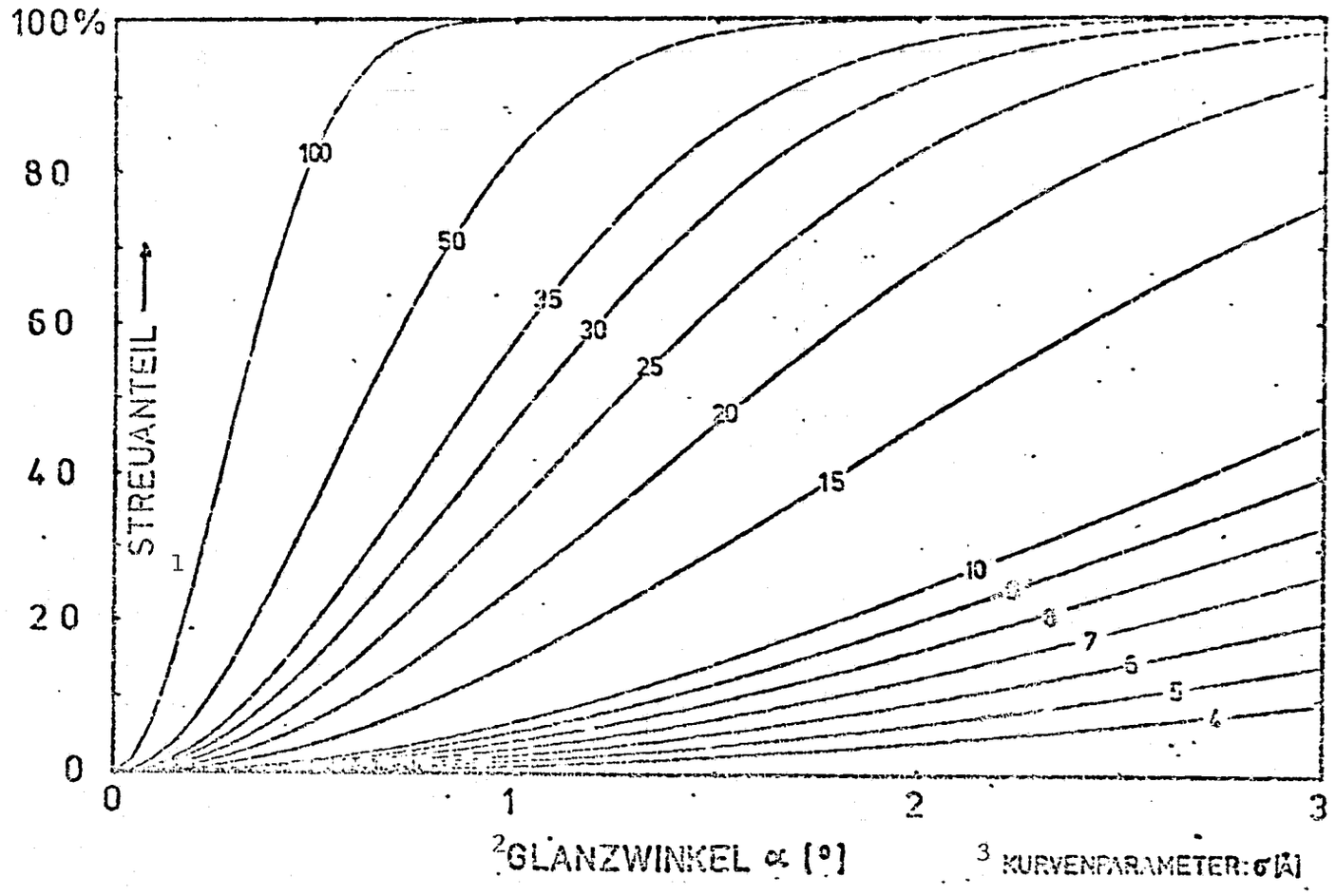

Figure 2: Dependence of the integral scattering angle on the angle of incidence for λ = 8.3 Å for simple reflextion (curve parameter: microroughness σ [Å])

Key: 1-Scattering angle 2-angle of incidence 3-curve parameter

2. The Operation of the Wolter Telescope and Specification for the 32 cm Telescope

/8

2.1 The Principle of the Wolter Telescope

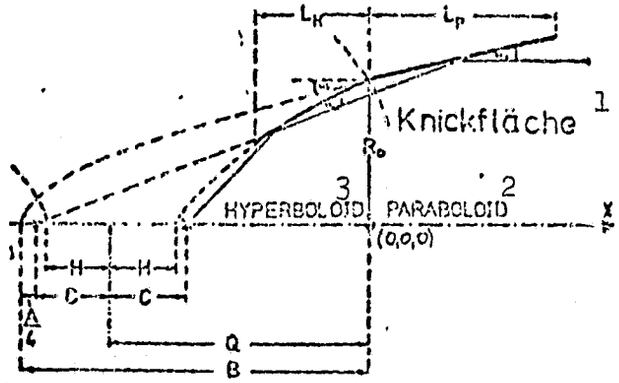

R_o	α	A	B	C	Q	H	L_p	L_H
150.	1.5	7.8	2854.1	717.5	2144.7	715.5	430.	360
mm	Deg.	mm	mm	mm	mm	mm	mm	mm

Figure 3: Basic Design of the Wolter Telescope with Parameters for the 32 cm Telescope

Key: 1-Bending Surface 2-Paraboloid 3- Hyperboloid

Since the refractive index of x-rays is very near to 1 for all materials ($n = 1 - \delta - i\beta$; $\beta, \delta \sim 10^{-6}$) (6) and $n < 1$, it is practically impossible to construct optic imaging systems for this range from standard lenses. The attempt to compensate for this property by a sufficiently large number of lenses would fail due to the severe absorption. However, it is possible to totally reflect x-ray radiation at surfaces if they are struck at an angle α which is smaller than a certain critical angle α_o to the surface.

The condition for total reflection is thus (6):

/9

$$\alpha \leq \alpha_o$$

Figure 4: Nomenclature

The angle α_0 is approximately given by:

$$\alpha_0 \approx \sqrt{2\delta}$$

when the complex refractive index is:

$$n = 1 - \delta - i\beta \qquad \delta, \beta : \text{optic constants of the material}$$

In principle we are studying the passage of x-rays from a vacuum (n=1) to a surface ($n \neq 1$).

Since the refractive index is not constant but depends very much on the wavelength and material, only a part of the total incident intensity is reflected--in contrast to the meaning of the concept "total reflection"--and the intensity ratio is given by (6):

$$\frac{I}{I_0} \approx \frac{(\alpha - a)^2 + b^2}{(\alpha + a)^2 + b^2} \qquad 2.1$$

with $$a = \left(\frac{1}{2}\left[\sqrt{(\alpha^2 - 2\delta)^2 + 4\beta^2} + (\alpha^2 - 2\delta)\right]\right)^{1/2}$$

and $$b = \left(\frac{1}{2}\left[\sqrt{(\alpha^2 - 2\delta)^2 + 4\beta^2} - (\alpha^2 - 2\delta)\right]\right)^{1/2}$$

As a reflection coefficient R we define the right side of (2.1); the wavelength dependence is found in the optic constants δ and β. As a most interesting example, we present the reflection coefficient of gold:

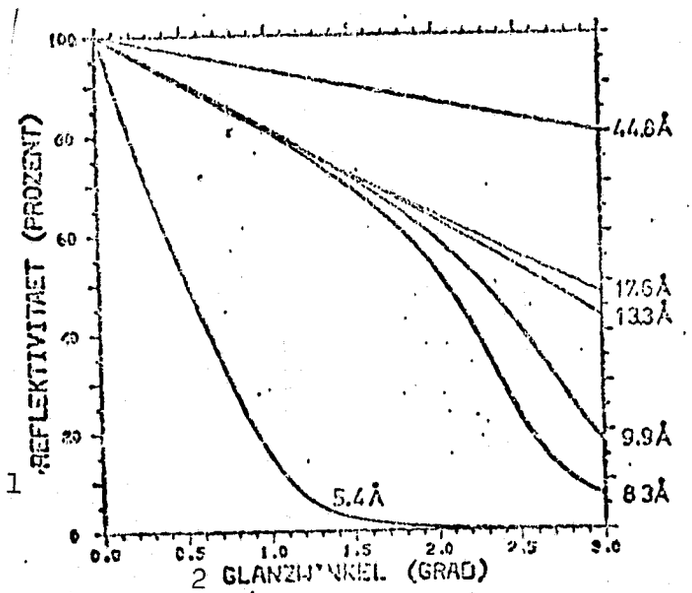

/10

Figure 5: Dependence of REflectivity on Angle of Incidence and Wavelength for Gold

Key: 1-Reflectivity (percent) 2-Angle of incidence (degrees)

Therefore gold is the most important material because it is stable over time and easy to vapor coat and because it does not have the pronounced edge absorption structure like nickel at the optimum energy for the 32 cm telescope, namely 1.5 KeV.

But now we know that a rotation paraboloid combines axis-parallel incident radiation into one point, the focus. Now if we take such a "slender" paraboloid so that the angle of incidence--that is the angle between the incident beam and the tangential plane to the paraboloid at the point of contact--is smaller than the boundary angle α_o, then total reflection takes place and the radiation is combined at the focus. Therefore it is possible to use a rotation paraboloid as imaging lens for x-ray radiation. But at the same time a severe difficulty arises: the Abbesche sine condition is treated roughly by such a system (5):

/11

Figure 6: The Abbeschen Sine Condition for Rotation Paraboloids

It is:

$$r = \frac{h}{\sin r} = \text{const.} \qquad 2.2$$

i.e., the bending surface, or the surface at which the extended, axis-parallel incident beams intersect the rearwards extended incident beams, should be a sphere about the focal point. But this requirement is treated roughly, particularly for a slender paraboloid. The bending surface is the paraboloid itself. In order to correct this error, it is never sufficient to use only a single-part paraboloid, no matter how it is shaped, if the condition for oblique incidence is to be met simultaneously. H. Wolter discovered in 1951 (5, 13) that this deficiency can be corrected if we connect a rotation hyperboloid to the rotation paraboloid; this hyperboloid has a rear focal point which coincides with that of the paraboloid. This is the Wolter Type I telescope (see Figure 3).

Now if the equations for:

2.3 Paraboloid $\quad R = \sqrt{A(X + B)}$ and

A,B,C,H,Q: Constants

2.4 Hyperboloid $\quad R^2 = (C^2 - H^2)\left((X + Q)^2/H^2 - 1\right)$

so according to an interim calculation we have:

$$2.5 \qquad r = \frac{A}{2} \cdot \left(\frac{Q^2 + H^2}{(C^2 - H^2)^2}\right) + X_1 \left(\frac{-Q - H}{C^2 - H^2}\right)^2$$

here, X_1 is the abscissa of the point of intersection of the incident ray and r is the distance of the focus to the point on the bending surface.

We see that r is not dependent on x_1, however, the factor at x_1 becomes smaller as the hyperboloid becomes slimmer. If we calculate from the bending surface, then we also have a rotation paraboloid as indicated in Figure 3. Since the paraboloid can be approximated by a sphere near the axis, a similar imaging quality is expected as from a parabolic mirror near the axis. /12

Radiation incident to the front undergoes a second reflection at the rear hyperboloid end; is incident near the bending point and is reflected a second time from near the bending point. In order to design the telescope as efficiently as possible, an attempt is made to have the collector surface area as large as possible with regard to the projected surface area of the paraboloids. (Singlely reflected beams must not be allowed into the detector). Now the projected surface gets larger with increasing angle of incidence, but the reflection coefficient decreases. So in order or maximize the effective surface area $F_{eff} \sim R_2 \cdot F_{geo}$ (this is decisive), an optimization between geometic collector surface area and reflection coefficient is needed, whereby the resolution, field of vision and energy range of incident radiation must be considered. From this we derive the angle of incident α which is 1.5° at the bending point for the 32 cm telescope since the effective surface area for $\lambda = 8.3$ Å has a maximum at 1.5°. The geometric collector surface area of the mirror is 106.042 cm^2, and this in turn, is determined by the telescope diameter, the telescope length and the angle of incidence. Since the 32 cm telescope is to be carried aloft by a Skylark carrier booster rocket, the maximum diameter of 32 cm will determine the size of this rocket.

The data of the 32 cm telescope are summarized below: /13

Maximum Diameter (inside)	321.717 mm
Diameter at the Bending Point	300.000 mm
Minimum Diameter	239.378 mm
Nominal Angle of Incidence at the Bending Point	$\alpha = 1.5^\circ$
Nominal Focal Width	1427.155 mm
Length of the Paraboloids	430.000 mm
Length of the Hyperboloids	380.000 mm
Surface	Gold (vapor coated)
Geometic Collector Surface Area	106.042 cm^2
Scattering Angle	<2x12 % for $\lambda = 8.3$ and $\alpha = 1.5^\circ$
Field of Vision	1°
Resolution Ability	20 arcsec FWHM

2.2 Imaging Error of the Wolter Type I Telescope /14

The imaging error of a Wolter Type I x-ray telescope is determined by the Seidel iconal and these errors are of third and higher order (13, 17, 2). The third order errors are treated, the higher order

errors are neglected. The following flaws will be discussed separately here, but naturally they can coincide for the telescope:

1. Spherical Aberration

2. Coma

3. Astigmatism

4. Distortion

We are assuming an aberration curve, that is, the curve of the image plane, obtained by taking all rays from one object point which passed through the outlet pupille (radius r_o).

1. Spherical Aberration

The aberration curves are concentric circles about the Gauss image point and its radius increases with $\sim r_o^3$, they are dependent on the location of the object in the field of vision.

2. The Coma

If Y and Z denote the cartesian coordinate axes perpendicular to the optical axis and y_o the distance of the object from the optical axis, then the aberration curves are given by :

$$\Delta y = - \text{const.} \; \sigma^2 y_o \, (2 + \cos 2\varphi)$$
$$\Delta z = - \text{const.} \; \sigma^2 y_o \sin 2\varphi$$

where ϕ is the azimuth angle. Therefore they are circles of radius const. $\sigma^2 y_o$ whose midpoints are shifted by -2 const. $\sigma^2 y_o$ to the Gauss image point (see Figure 7).

/15

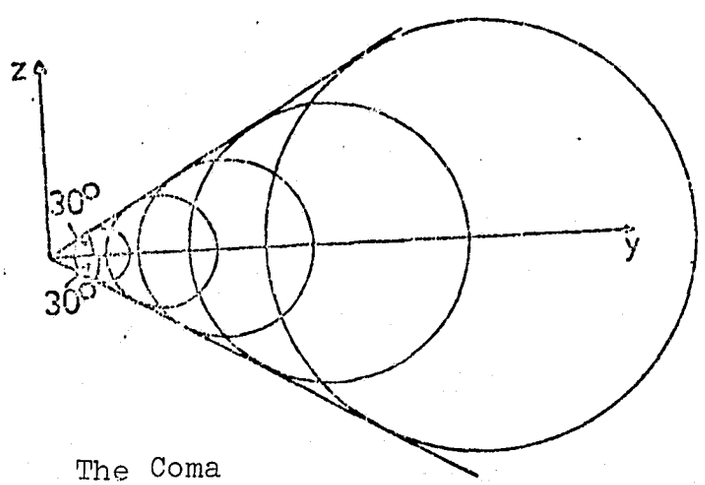

Figure 7: The Coma

These errors give the images an asymmetric, tailing appearance whose name is taken from the terminology used for comets.

3. The Astigmatism

An incident, thin bundle of rays has two focal lines, one radial (sagittal) to the axis of the telescope, another tangential to a circle whose midpoint lies on the optic axis and whose surface is normal to the optical axis (meridional). If we shift the object in the object plane, then they pass through the sagittale or meridionale image area. These surfaces can be replaced closely by two spheres which are in contact at the axis. Their radii are (17):

$$\frac{1}{\rho_M} = 2n\,(2C + D) \qquad \text{n: Refractive Index}$$

$$\frac{1}{\rho_S} = 2nD \qquad \text{C,D: Constants}$$

One half the difference in bending is:

$$\frac{1}{2}\left(\frac{1}{\rho_M} - \frac{1}{\rho_S}\right) = 2nC$$

This is now called the astigmatism. It causes an elipse-shaped blurring in the image plane.

4. The Distortion

/16

If the object lies on the y-axis (that is, $z_o = o$), the deviation from the Gauss image point for the general occurrence of this error is:

$$\Delta y = - \text{const.}\; y_o^3$$
$$\Delta z = o$$

With the Wolter telescope the constant is positive which results in a cylindrical distortion (see Figure 8).

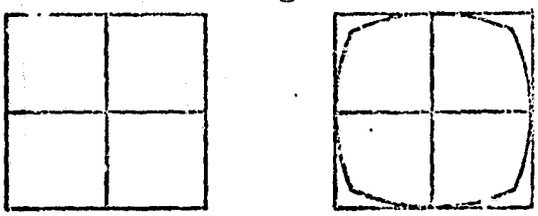

Figure 8: Distortion

The errors that we have discussed up to now are system-induced and also occur for an"ideal"telescope. For a "real" telescope, additional fabrication-induced errors occur (15).

A. Faults in the Individual Mirrors

1. Deviation from Nominal Radius $|\bar{r} - r_c| = \delta_o$
2. Deviation from Nominal Radii Difference $|(\bar{r}_2 - \bar{r}_1) - (r_2 - r_1)| =$
3. Deviation from Circular Form in the Azimuth Direction $|(r_i(\phi) - \bar{r}_i)| = \delta_2 \quad (i = 1,2)$
4. Deviation from Radii Difference (Azimuth):

$$|(r_2(\phi) - r_1(\phi)) - (\bar{r}_2 - \bar{r}_1)| = \delta_3$$

5. Deviation for Nominal Meridian Line = Tangent Error = δ_4
6. Microroughness δ_5

B. Fault in the Mounted Telescope /17

1. Tipping of the Axes of Paraboloid and Hyperboloid = δ_6
2. Shifting an Axis of One Element Perpendicular to the Optic Axis = δ_7
3. Shifting the Axis of One Element Parallel to the Optic Axis = δ_8

Faults A1, A2 and B3 only result in a shift in the focal plane, whereas the effect of A2 is the most severe. But these flaws are of no great significance for the resolution ability since they can be compensated by shifting the image plane.

A3 is also not too critical for the resolution ability, whereas A4 decreases it typically by a factor of $\frac{2(f+L_p)}{L_p}$ more than A3.

The alignment errors, that is, slowly oscillating deviation from the theoretical meridian line with amplitudes of several μ, have a quite severe effect on the resolution ability since they are included directly in the width of the point image by changing the angle of incidence. Correlation lengths occur which depend typically on the polishing tool etc.

The microroughness, that is, quickly oscillating deviations from the theoretical meridian line with amplitudes of several Å, which remain even for high polished surfaces, leads to an enlargement of the scattered fraction at one profile point and thus causes primarily a reduction in contrast.

B1 causes radiation incident parallel to the axis of the hyperboloids to be focused within a narrow ring whose midpoint lies at $-\vec{r}$ whereby $\vec{r}$ is the intersection of the paraboloid axis with the focal plane when (o,o) is the intersection of the hyperboloid axis with the focal plane.

B2 causes focusing of paraxial radiation in a ring whose diameter is about equal to the shift and whose midpoint coincides with the optic axis of the hyperboloids.

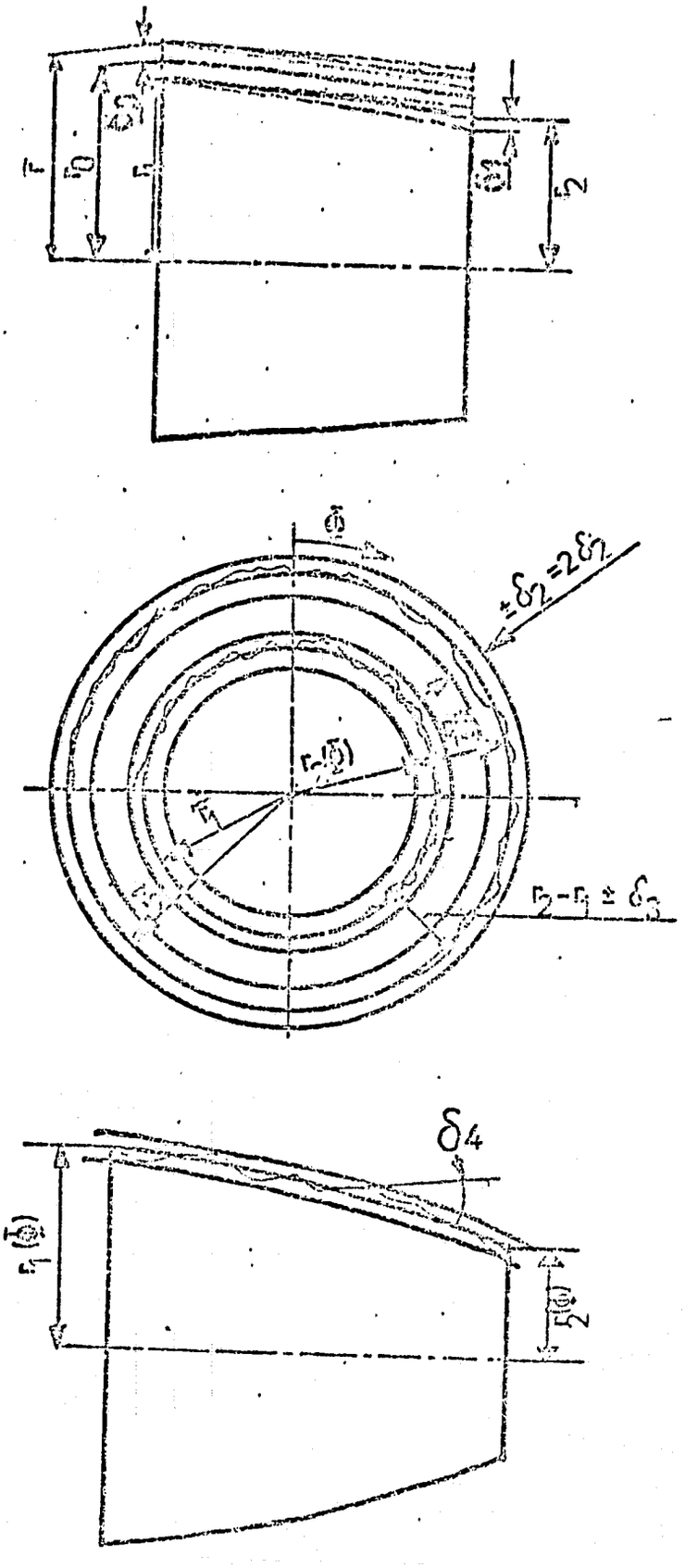

Figure 9/1: Nomenclature of Fabrication-Induced Imaging Errors

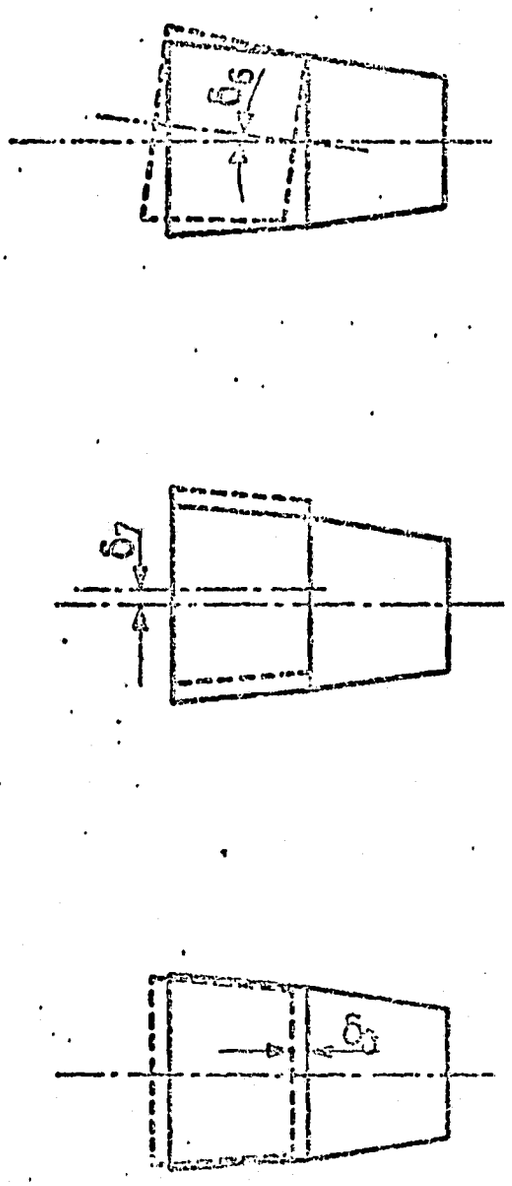

Figure 9/2: Nomenclature of Fabrication-Induced Imaging Errors

For the 32 cm telescope however, not all these quantities are specified individually, but only a resolution of 20 arcsec and a scattering fraction of $< 12\%$ at $\lambda = 8.3$Å is desired and this results from the scientific objective of the experiment--namely, the observation of astrophysical dust-scattering halo. /20

2.3 Off Axis Behavior of the Wolter Telescope /21

We proceed from an "ideal" telescope, i.e. a telescrope whose surface ridgidly follows the mathematical functions. In this case a axis parallel incident bundle is focused at one point. If a parallel bundle has an angle opposite the optic angle, then the image in the focal plain is a distortion figure near the Gauss image point whose diameter is small compared to the deviation from the optic axis. The resolution ability of the telescope is determined by this diameter and it is optimum when the image plane is bent. In (4), an empirical approximation formula found by L.P. Van Speybroeck and R. C. Chase is given for the RMS blur circle radius of a Wolter Type I telescope:

$$\sigma_D = \frac{1}{5}\,\frac{\varepsilon^2}{\alpha}\left(\frac{L_p}{f}\right) + 4\varepsilon\alpha^2$$

with:
- σ_D : RMS Radius of the Point Image Function for Optimum curved Image Surface
- ε : Off Axis Angle
- α : Angle of Incidence
- L_p : Length of the Paraboloids
- f : Focal Length of the Telescope

But since today no x-ray detectors with bent sensitive surfaces are available, this radius must be determined for a flat image surface. From ray tracing programs we obtain the following profile (14) for the 32 cm telescope:

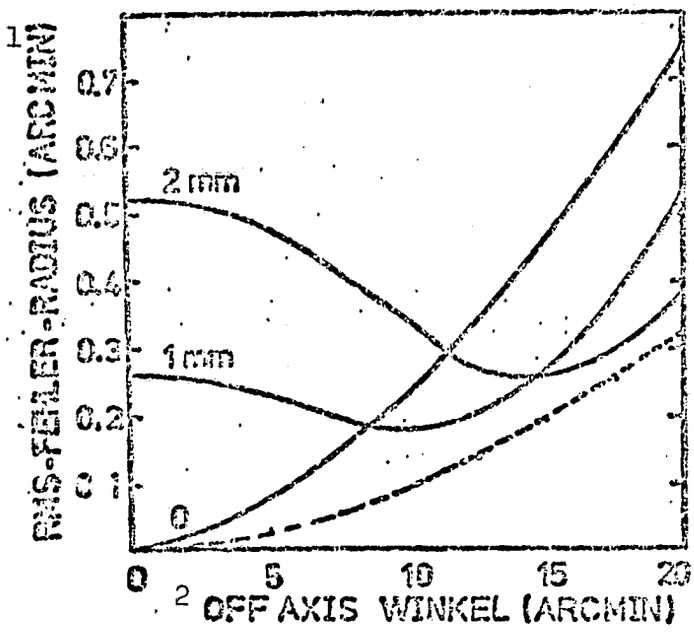

Figure 10: Resolution ability of the 32 cm telescope as a function of off axis angle. Approximation from Van Speybroeck

Key: 1-RMS Error Radius (arc min) 2- Off Axis Angle (arc min)

The curve parameter is the shift of the image plane from the nominal focus to the telescope. As we see from the drawing, the RMS radius increases constantly for d = o with increasing off axis angle ($\sigma_2 \approx c_1 c + c_2 c^2$) for d ≠ o the curves show a minimum. Therefore, by shifting the image plane to the telescope for a certain off axis angle, the resolution ability can be optimized, however this improvement is achieved at the expense of the on-axis resolution ability. Figure 11 (14) shows the intensity distribution in the point image for various off axis angles and image planes. We see that for each off axis angle the intensity becomes a maximum for a certain shift within a fixed radius and that this is particularly true for increasing shifts d.

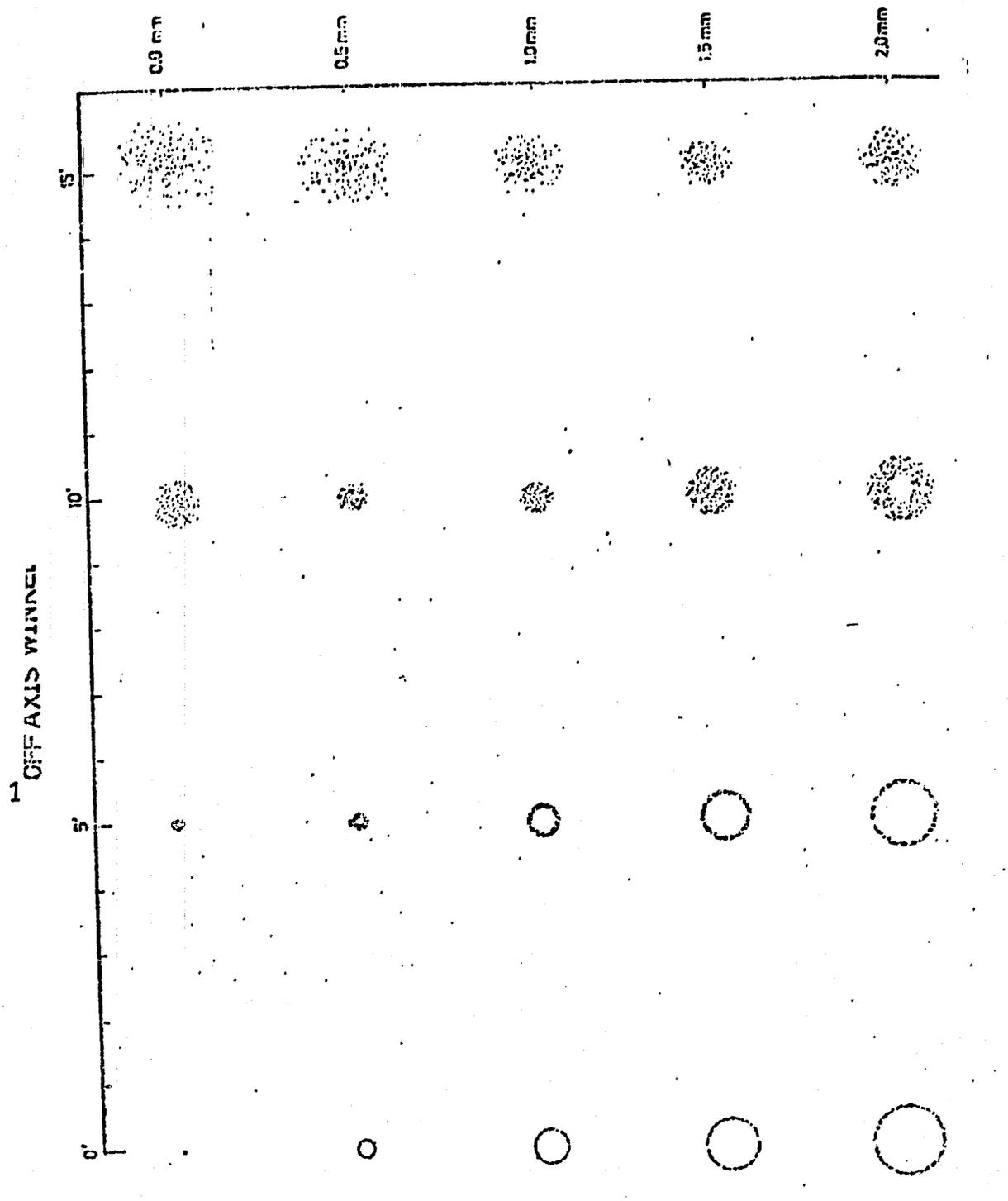

Figure 11: Intensity distribution in the point image for different off axis angles and positions of the detector plane in a geometic-optic approximation.

Key: 1-Off Axis Angle

2.4 Discussion of Reflectivity /24

As we have already shown in Section 2.1, total reflection takes place in a region of weak x-ray radiation only for angles of incidence smaller than a certain limiting angle α_o which typically lie on the order of 1^o. The reflection coefficient is determined by the complex refractive index $n = 1 - \delta - i\beta$ etc. Since in the present study, the reflectivities of gold and nickel (Kanigen is nickel phosphide, 90% Ni, 10% P) have been studied, the optic constants of these materials are presented in the following table:

	Gold			Nickel		
λ [Å]	δ	β	α_o	δ	β	α_o
5.4	$1.4 \cdot 10^{-4}$	$1.1 \cdot 10^{-4}$	0.96	$3.6 \cdot 10^{-4}$	$8.6 \cdot 10^{-5}$	1.54
8.3	$9.0 \cdot 10^{-4}$	$2.2 \cdot 10^{-4}$	2.43	$7.8 \cdot 10^{-4}$	$3.4 \cdot 10^{-4}$	2.26
9.9	$1.2 \cdot 10^{-3}$	$3.4 \cdot 10^{-4}$	2.80	-	-	-
13.3	$2.4 \cdot 10^{-3}$	$1.1 \cdot 10^{-3}$	3.96	$9.3 \cdot 10^{-4}$	$1.5 \cdot 10^{-3}$	2.47
17.6	$3.7 \cdot 10^{-3}$	$2.4 \cdot 10^{-3}$	4.92	$1.4 \cdot 10^{-3}$	$5.9 \cdot 10^{-3}$	3.73
44.8	$2.1 \cdot 10^{-2}$	$9.9 \cdot 10^{-3}$	11.61	$1.5 \cdot 10^{-2}$	$1.5 \cdot 10^{-2}$	9.93

The values given here will be used below for optical constants. These were taken from B. Aschenbach (14).

But now R also depends on the angle of incidence α (see Figure 5). However, since the 32 cm telescope has angles of incidence at the paraboloids α_p and hyperboloids α_H which are nearly equal ($\sim 1.5^o$) and since they vary only a little over the particular mirror lengths, for the reflected intensity we expect the following:

$$I_{ref} = R_p \cdot R_H \cdot I_o \approx R^2 \cdot I_o$$

However, this is true only far from the absorption constant of the reflecting medium.

2.5 Scattering at the Wolter Telescope /25

Every optic surface no matter how well polished, is never completely smooth, there is always a so-called"microroughness". With present methods this can certainly be reduced to height differences up to several ten Å, however, this is not negligible if we wish to reflect electromagnetic waves with wavelengths of 5 ÷ 50 A from it. Now if we let a plane wave fall on such a rough surface, the incident wave will no longer be a plane wave and intensity is bent in angle ranges beyond the specular direction. In order to describe this scattering behavior, a model was developed by P. Beckmann (7), (14) which uses a statistic, rough surface as a basis.

The surface is described by two statistic functions:

1. The elevation distribution w(z) which denotes the probability that

elevation z will occur on a surface and

2. The autocorrelation function $c(\tau)$ which is defined as $\sigma(\tau) \frac{\langle h(x_1,y_1) \cdot h(x_2,y_2) \rangle}{\langle h^2(x_1,y_1) \rangle}$

with $\tau = \sqrt{(x_1-x_2)^2 + (y_1-y_2)^2}$ where h (x,y) represents the surface.

Now if we assume--as has been confirmed by measurements-- that w(z) is normally distributed, that it is $w(z) = w(z) = \frac{1}{\sigma\sqrt{2\pi}} e^{-\frac{z^2}{2\sigma^2}}$ then after longer intermediate calculation (14) we find that the scattered fraction of the intensity is

$$I_{St} = I_o (1 - e^{-(2k\sin\alpha\sigma)^2}) = I_o(1 - e^{-q})$$

where k is the wave vector of the incident wave and α is the angle of incidence. This result is completely independent of the autocorrelation function c (τ) and permits statements on the microroughness merely from scattering measurements.

Now we can certainly draw conclusions from scattering measurement about the elevation distribution w (z), however we still do not know how the mountains and valleys are distributed over the mirror surface. For this, we must make assumptions for the autocorrelation function.

Optical measurements (16) suggest an exponential law: /26

$$c(\tau) = e^{-\frac{|\tau|}{\tau}}$$

With this, the scattered intensity I_{St} is:

2.5.1 $$I_{St} \propto \sum_{m=1}^{\infty} \frac{g^m}{m!\,m} \frac{1}{1 + (\vartheta/\vartheta_m)^2} \qquad \text{with} \quad \vartheta_m = \frac{m}{kT\tau}$$

whereby ϕ denotes the scattering angle. In the following measurements, it is related to a focal width of 3,077 mm for paraboloids and to 1,427.2 mm for the total telescope.

With the Wolter Telescope we now have two reflections so that the incident energy is divided up as follows:

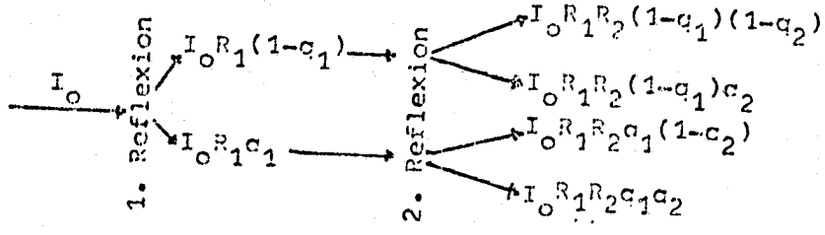

q_i: Scattering fraction of the i-th reflection

The entire scattered fraction is thus: $\frac{I_{St}}{I_o} = q_1 + q_2 - q_1 q_2$.

For small q, that is, slightly scattering surfaces, we have $\frac{I_{St}}{I_o} \sim q_1 + q_2$, that is, twice the fraction as for one reflection.

Within the framework of his doctoral dissertation, R. Lenzen studied plane samples(also prepared by C. Zeiss Company) for their scattering behavior (14). Here, sample numbers 27 and 29 had a scattering of 30% or 2% corresponding to 15 Å or 4 Å at $\alpha = 1.5^o$ and $\lambda = 8.3$ Å. Since with the 32 cm telescope, astrophysical dust scattering halos are to be measured, the requirement results that the experimental halo must clearly lie below the astrophysical halo. This requirement is met by the specification that the surface of the telescope must lie between samples 27 and 29.

The selection of a metal mirror was made primarily for two reasons: /27

1. We could rely on experiences of the preceding ASTRO-8 experiment and
2. The attendant theory confirmed by the work of Lenzen (14) was known.

2.6 Defraction at the Wolter Telescope

If--as described in Section 4 of this paper--one wishes to test a Wolter telescope in the optic wavelength range, then the diffraction of the incident wave at the given apertures must be considered. Initially, we have the diffraction at the paraboloid surfaces which practically represents a circular aperture: (1, 8, 9, 10, 11, 12)

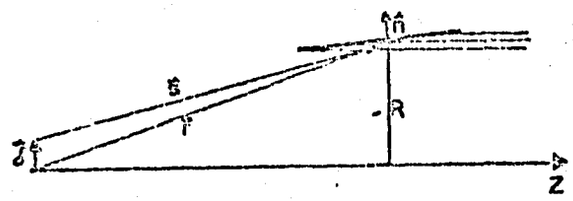

Figure 12: Diffraction at the Paraboloids

The resulting diffraction figure is, strictly speaking, bent again at the circular aperture of the hyperboloids, however, only a close aproximation shall be given here so that we can neglect this and consider only that the deviation δ is diminished in the focus of the telescope compared to the deviation δ in the focus of the paraboloid by the factor $\frac{f_{Tel}}{f_{par}}$, whereby f_{Tel} is the focal width of the telescope and f_{par} is that of the paraboloids.

We therefore calculate the diffraction pattern of the paraboloids. /28 For this, we proceed from the Kirchhoff-Integral (1):

$$U(\delta) = \frac{1}{4\pi} \iint_S \left(u \left(\frac{\partial \psi}{\partial \hat{n}} \right) + \psi \left(\frac{\partial u}{\partial \hat{n}} \right) \right) d\vec{S}$$

with $u = 2E_1 e^{ikr}$

and $\psi = \frac{e^{-ikrs}}{s}$

S is the surface area of the paraboloids, dS is the surface element on it, $\vec{n}$ is the normal vector to the surface at the field point, U is the incident plane wave and ψ is the exiting spherical wave. Under the assumption that $r \sim s$, which is very nearly met in the present case, the integral is evaluated and we obtain:

$$u(\delta) = \frac{ikG_0}{\lambda} \int_{R_1}^{R_2} J_0\left(\frac{k\delta R}{r}\right) \frac{(R^2 + AB)R}{r^2} dR$$

when the equation of the paraboloids is: $R^2 = A(Z+B)$.

This integral was evaluated numerically for $\lambda = 5,000$ Å, the result is shown in Figure 13. The image is pronounced by two oscillating functions, whereby the fast one is caused by the circular aperture of the telescope with $2R_2$ diameter and the slower one is caused by the circular slit of width $R_2 - R_1$. If we now implement the change in scale according to:

$$\delta' = \delta \cdot \frac{f_{rel}}{f_{tat}}$$

then in close approximation we obtain the diffraction pattern in the focal plane of the telescope (see Figure 14).

Now if we wish to prevent radiation from moving into the detector directly, that is, without reflection, we must install shutters. Therefore, at the rear opening of the 32 cm telescope, a circular shutter is attached which forms a circular slit 13 mm wide. A diffraction figure results here too and this will be calculated now. We again proceed from the Kirchhoff-Integral:

$$u(\delta) = \frac{1}{4\pi} \iint_S \left(u\left(\frac{\partial \psi}{\partial \vec{n}}\right) + \psi\left(\frac{\partial u}{\partial \vec{n}}\right)\right) d\vec{S}$$

δ is again the deviation from the optical axis, $U = 2E_1 e^{ikr}$ is the incident plane wave, $\psi = \frac{e^{-iks}}{s}$ is the exiting spherical wave, S is the surface area of the round slit, n is the normal vector to it and dS is the surface element.

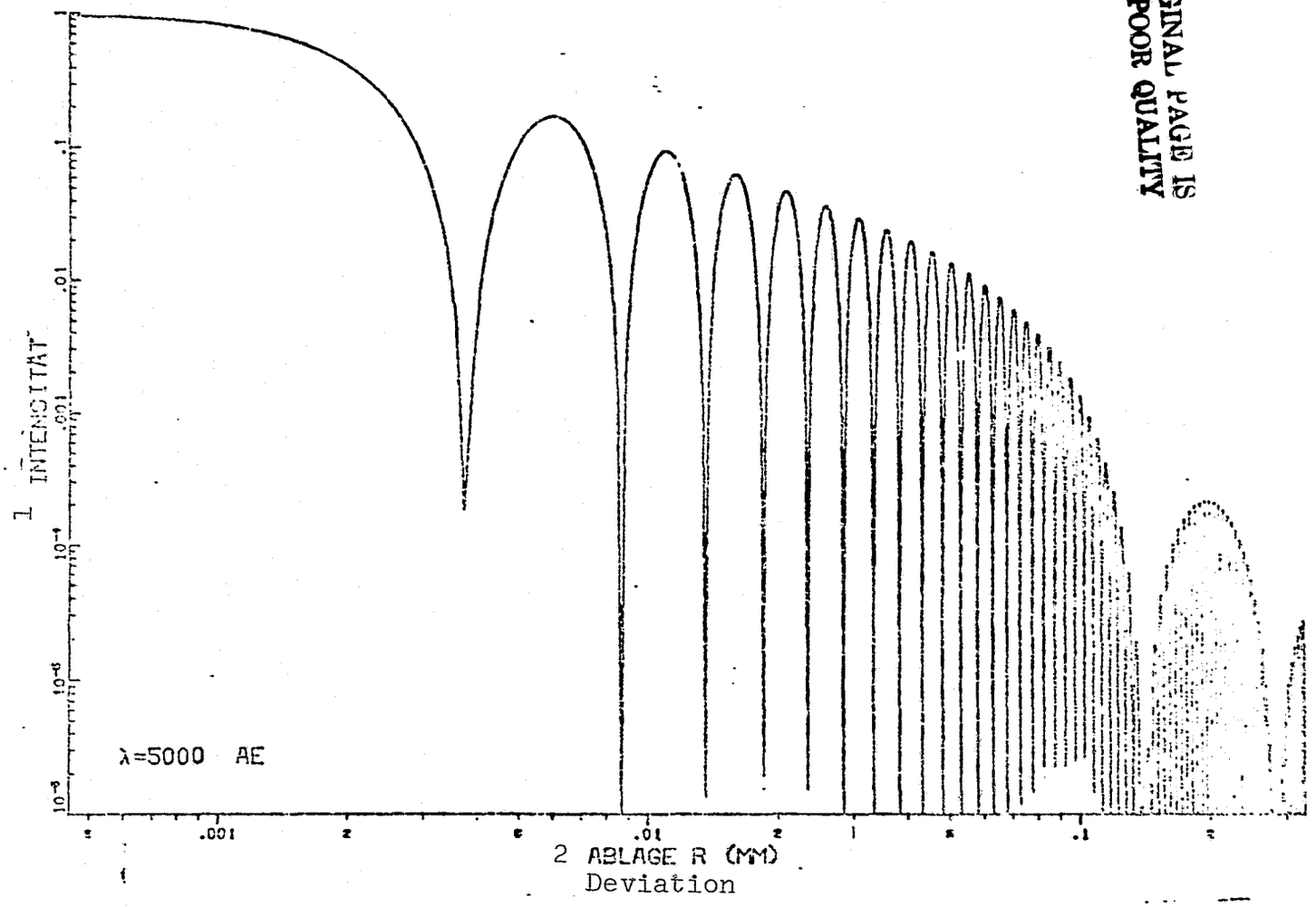

Figure 13: Diffraction pattern of the paraboloid in the parabola focus for λ = 5 000 A^{o} (intensity in the center is standardized to 1) as a function of the deviation R from the optic axis.

Key: 1-Intensity 2-Deviation

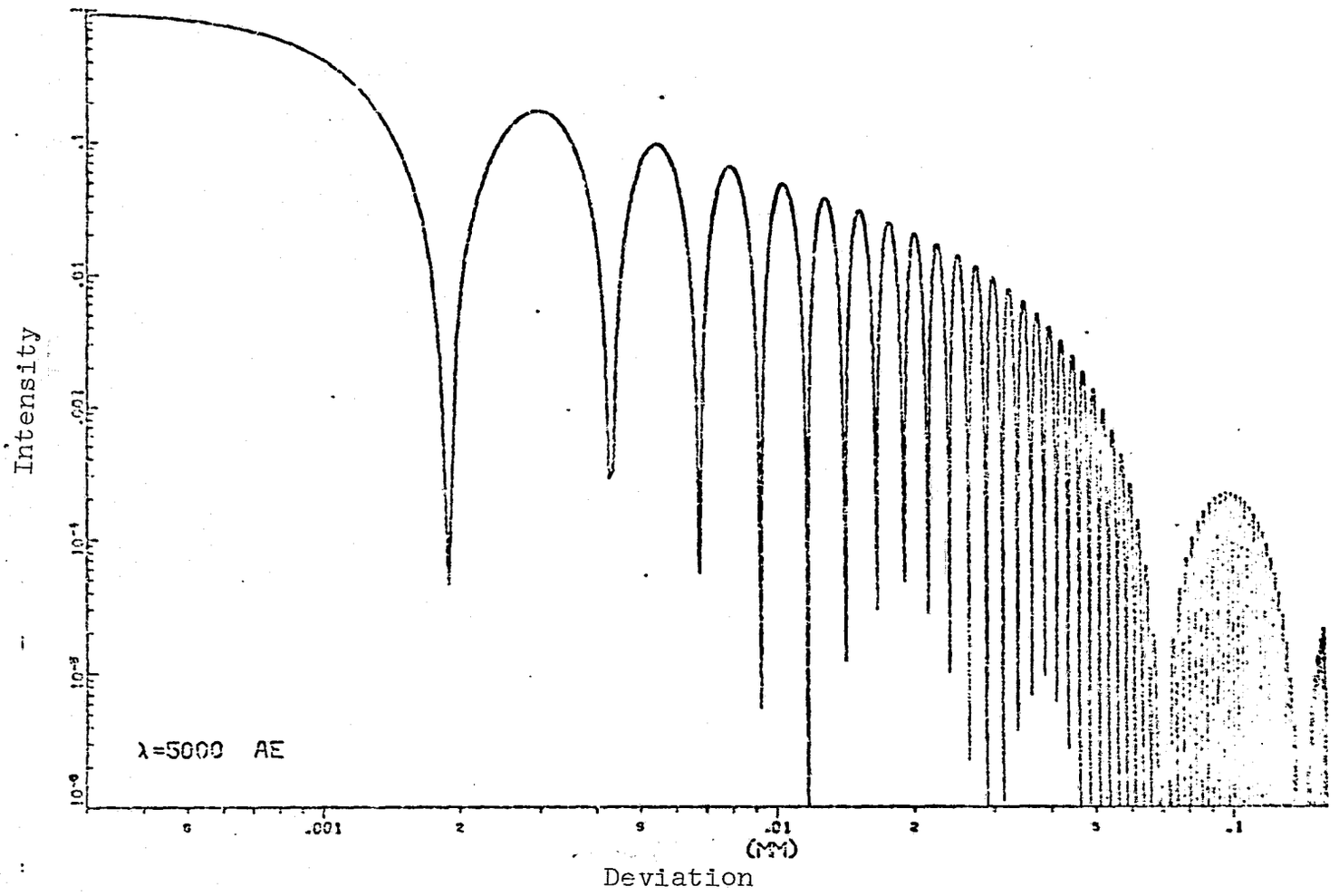

Figure 14: Diffraction pattern of the paraboloid in the telescope focus for λ = 5,000 A (intensity in the center is standardized to 1) as a function of the deviation R from the optic axis.

Then the conditions are illustrated as follows: /31

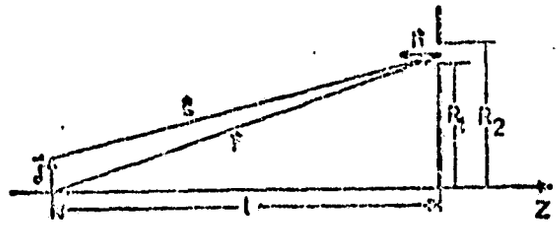

Figure 15: Diffraction at the circular slit

If we perform the first integration, then we obtain:

$$U(\delta) = -ikE_0 e^{ikl} \int_{R_1}^{R_2} J_0\left(\frac{k\delta R}{r}\right) \frac{dR}{r}$$

This was also evaluated numerically and is illustrated in Figure 16. The fast oscillation is again due to the circular aperture with diameter $2R_2$, the slow one is due to the "slit" $R_2 - R_1$. The diffraction pattern is thus composed of very nearly the diffraction figure at the paraboloids and circular slit.

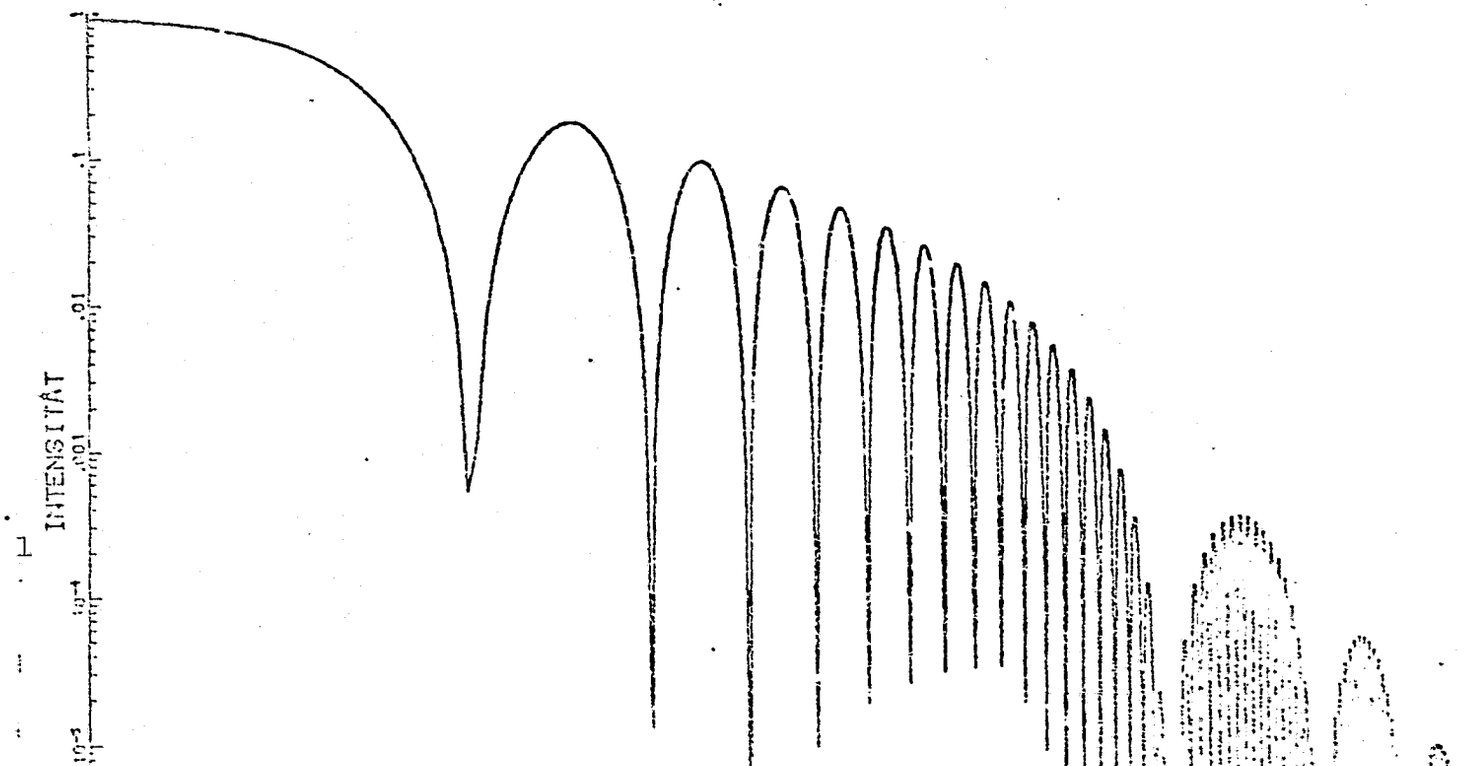

Abb. 16 Beugungsbild einer Ringblende der Breite 13 mm 1047.2 mm hinter dieser für λ = 5 000 Å (Intensität im Zentrum zu 1 normiert) in Abhängigkeit von der Ablage R von der opt. Achse

Figure 16: Diffraction pattern of a circular shutter 13mm wide located 1047.2 mm behind it for λ = 5 000 Å (intensity in the center is standardized to 1) as a function of the deviation R from the optic axis.

Key: 1-Intensity 2-Deviation

2.7 Behavior of the 32 cm Telescope for Divergent, Integral Illumination /33

In contrast to the preceding, we will now discuss x-ray optic properties of the 32 cm telescope.

Previously we have always assumed a parallel incident bundle. However, this condition cannot be created in the laboratory. Therefore, below we attempt to discover which image results behind the 32 cm telescope when it is illuminated by a divergent bundle with an opening angle of 2δ. The shutter at the rear aperture is included in this.

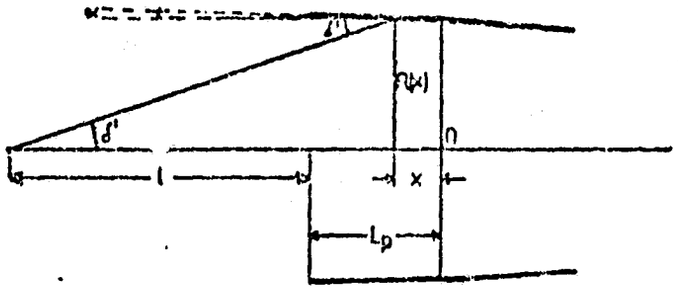

Figure 17: Divergent Illumination

If we set up a point source at the distance l from the front edge of the telescope along the optic axis, then the actual angle of incidence α changes according to:

$$\alpha' = \alpha + \delta'$$

$$\text{with } \delta' = \arctan\left(\frac{R(x)}{l + L_p - x}\right)$$

Now in order to obtain the intensity distribution in a plane perpendicular to the optic axis behind the telescope, a ray tracing program was developed which also considers the dependence of the reflection coefficient on the angle of incidence with the optic constants from Section 2.4 for gold. Here we assumed a $\cos^2$-shaped source profile and $\lambda = 8.3$A. The calculation was performed for $l = 15$ m and $l = 300$ m since test ranges of these lengths do exist. The results are illustrated in Figures 19 and 22. The resolution /34 is 0.01 mm corresponding to 1.45 arcsin in the focus. We see that even when $l = 300$ m where the angle δ is only 1.7 arcmin, a ring results in the focal plane. This is due to the fact that a divergent bundle is reflected from the hyperboloid and this bundle intersects behind the nominal focus. This effect is more pronounced the closer the source is to the telescope.

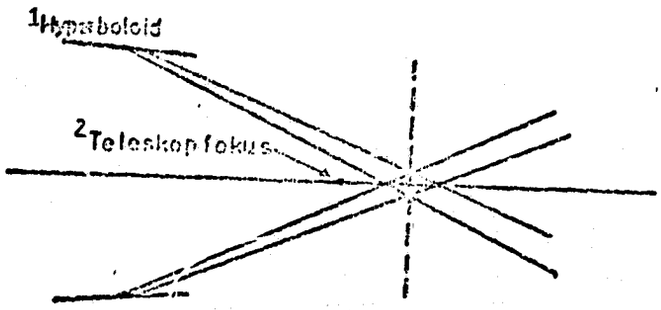

Figure 18: Divergent Illumination

Key: 1-Hyperboloid 2-Telescope Focus

As we see in Figure 18, there is one point where the diameter of the image has a minimum and this point depends on the distance of the source:

Table 1: OPTIMUM IMAGE PLANE AND ATTENDANT IMAGE DIAMETER AS A FUNCTION OF THE DISTANCE TO THE SOURCE

Distance to Source	Optimum Image Plane	Image Diameter
15 m	131.7 mm behind focus	2.5 arcmin
300 m	6.5 mm behind focus	2.9 arcsec

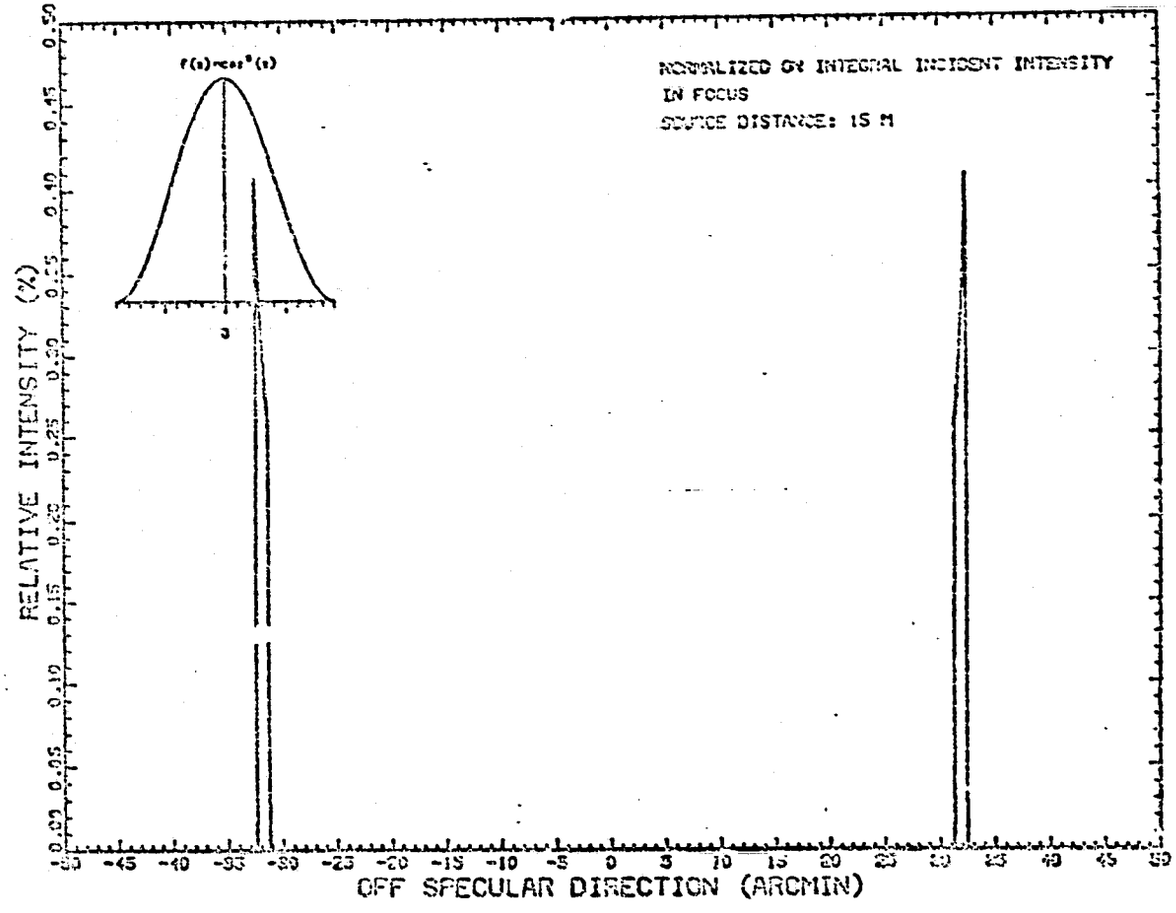

Figure 19: Intensity distribution in the focal plane of the 32 cm telescope for a source distance of 15 m and divergent illumination

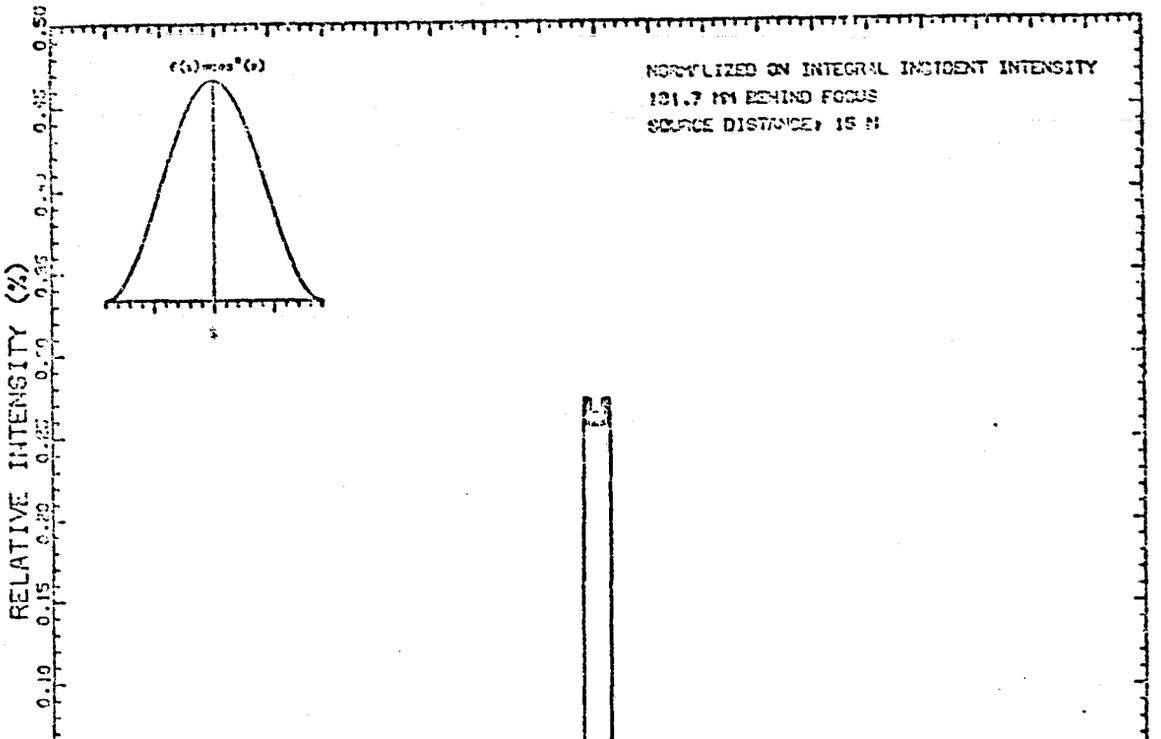

Figure 20: Intensity distribution in a plane 131.7 mm behind the focus of the 32 cm telescope for a source distance of 15 m and divergent illumination

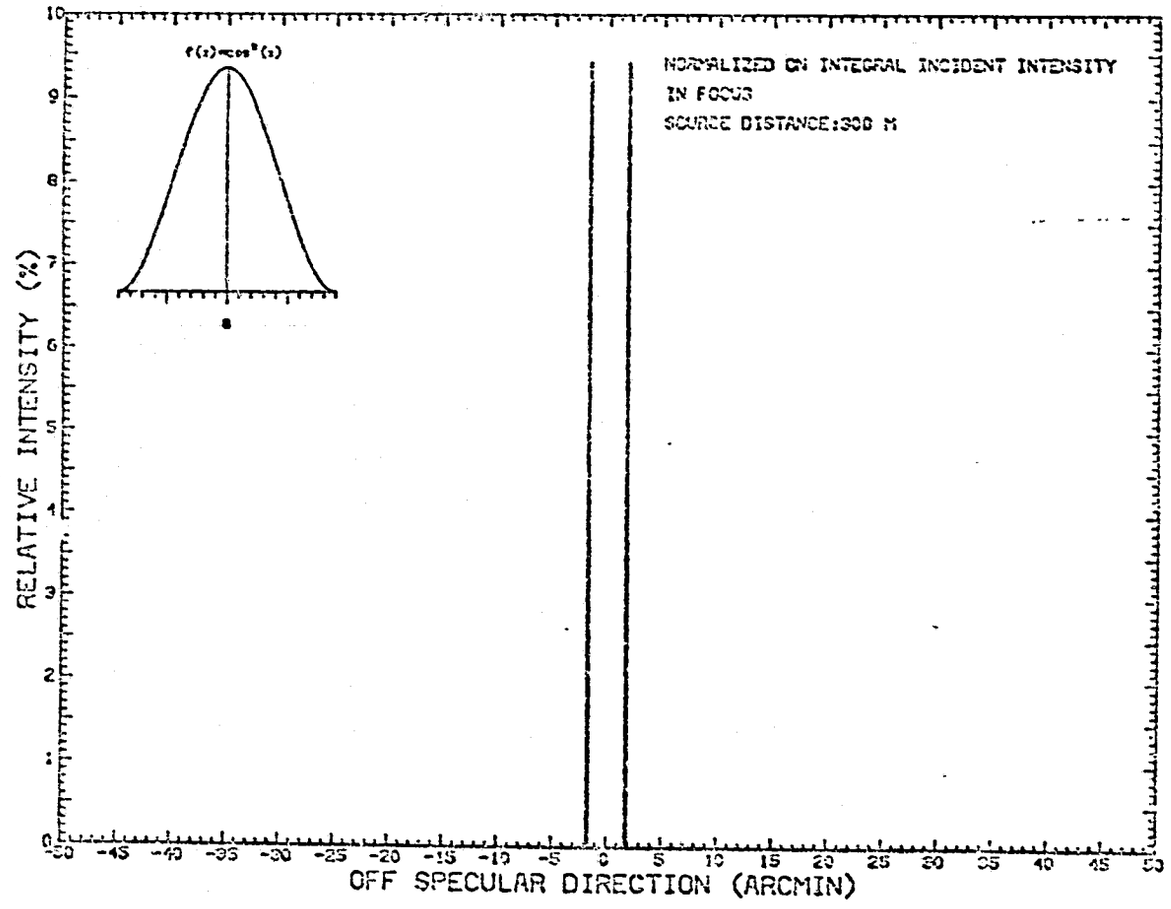

Figure 21: Intensity distribution in the focal plane of a 32 cm telescope for a source distance of 300 m and divergent illumination

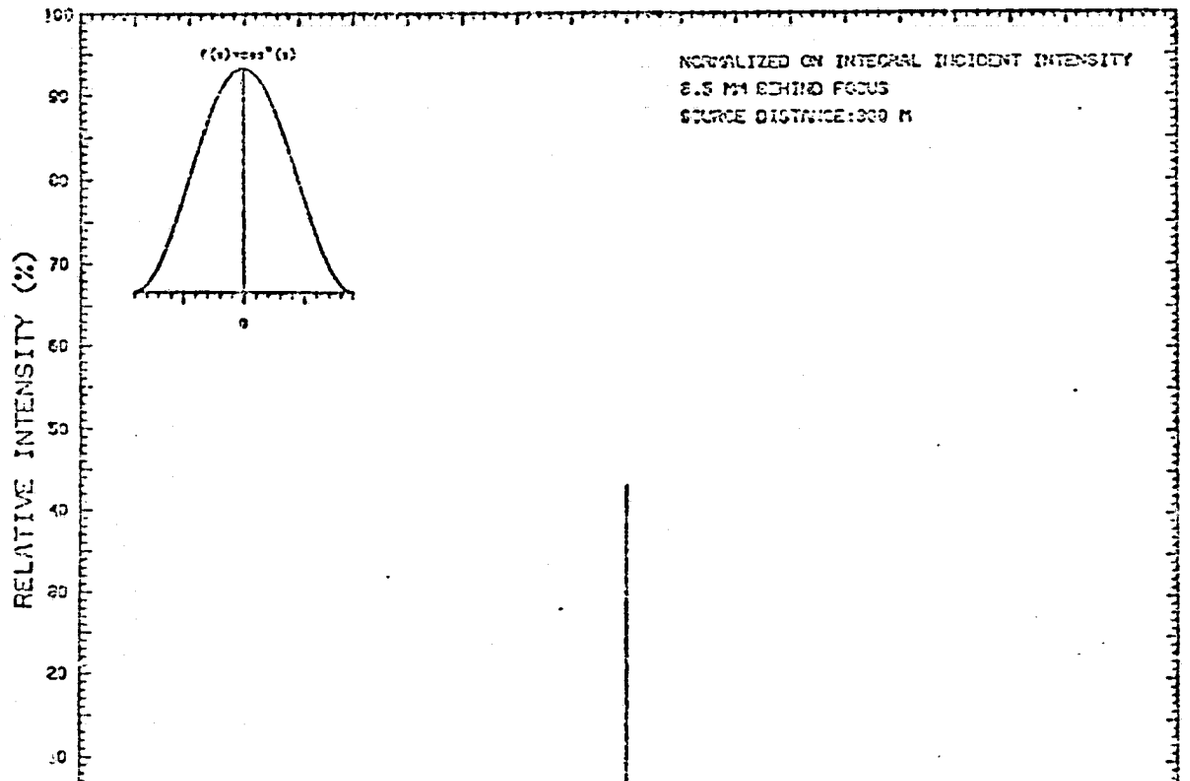

Figure 22: Intensity distribution in a plane at 6.5 mm behind the focus of the 32 cm telescope for a source distance of 300 m and divergent illumination

At this point we can check the extent to which the lens equation is met by the 32 cm telescope: /39

$$\frac{1}{a} + \frac{1}{b} = \frac{1}{f}$$

a: Width of the object
b: Image width
f: Focal length

When a = 300 m, we obtain a "b" of 6.8 mm at f = 1,427.2 mm. The optimum according to Table 1 is at 6.5 mm which gives a deviation of 4.6%. When a = 15 m, we obtain a "b" of 150 mm corresponding to a deviation of 12.2%. Therefore, the deviations are still quite small under consideration of the fact that we are dealing with a"thin" lens for which the equation is still valid.

Now the telescope shall be flown aloft in connection with a local resolution proportional counter which will have a resolution of 0.3 mm. Now one can ask how far the source must be in the test range in order to keep the point image diameter smaller than the resolution element of the detector. As a solution, the ray tracing program was used in slightly modified form and a distance of at least 33.7 m results when the image is observed at the optimum point. The point image diameter is exactly 0.3 mm for an image plane separation of 58.1 mm behind the nominal focus. But now we are interested not only in the point image diameter, but also in the expected intensity. Due to the fact that for this type of illumination the angle of incidence is basically greater than for paraxial illumination, the angle of incidence is also greater and a part of the reflected ray falls on the rear shutter. At 300 m this fraction is 3.4%; at 33.7 m it is 35.4% and at 15 m, 62.8%. These calculations could not be checked experimentally since the test system was not designed for this.

2.8 Behavior Under Hot and Cold Conditions /40

The 32 cm telescope will be part of a rocket payload to be launched from Australia. At the moment of launch, temperatures of about 40° C are expected. While the rocket is in count-down, it will heat up considerably so that some telescope deformation is expected. Therefore, the point image for various tempertures was studied. We make the following assumptions:

1. The imaging is optimum at 20° C.
2. There is paraxial incident rays.
3. The telescope is ideal.
4. The changes obey the law $l = l(1 + \alpha \cdot \delta T)$
5. $\alpha = 25.10^{-6}$ $(\frac{1}{grd})$ for the aluminum alloy used.

The image was again calculated with the ray tracing program from Section 2.7. If in addition, we consider the length change in the structure

connecting telescope and detector according to points 4 and 5 above, then we obtain the following result (see Figure 23):

TABLE 2: DEPENDENCE OF POINT IMAGE DIAMETER AND OPTIMUM IMAGE PLANE ON TEMPERATURE

T (° C)	Optimum Image Plane (mm)	Point Image Diameter (arcsec)
10	1 426.9	33.3
15	1 427.0	23.3
20	1 427.2	0.0
25	1 427.4	9.7
30	1 427.6	21.6
35	1 427.7	37.6
50	1 427.9	49.9

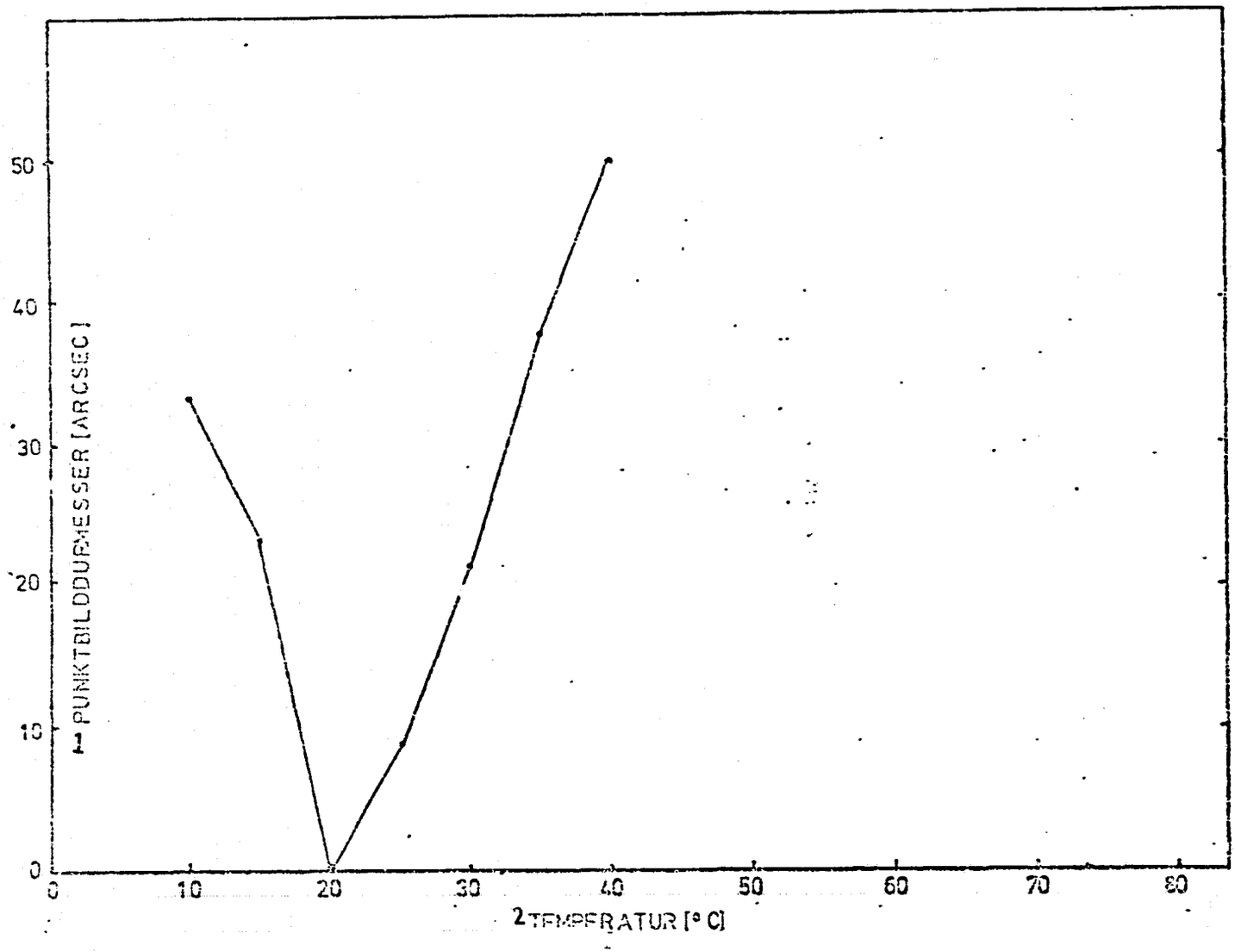

Figure 23: Dependence of the point image diameter for the 32 cm telescope on temperature under consideration of the structure

Key: 1-Point Image Diameter 2-Temperature

For a detector resolution of 0.3 mm = 43.3 arcsec it must be assured through appropriate measures that the payload does not get warmer than 35° C so that the resolution ability remains smaller than that of the detector. In addition, the calucation was performed for an ideal telescope and this is not actually available, i.e., the permissible temperature range must be further restricted if the resolution of the detector is to be increased by 0.2 mm (0.2 mm ≙ ≙ 28.9 arcsec ↛ 15° C < T < 30° C). /42

2.9 Comparison with Other Imaging Systems /43

Right in the beginning we can say that in many cases the Wolter telescope is preferred over other systems because of its superior properties.

If we think of an imaging system, our thoughts naturally turn to lenses known from the optical spectral range. However, since the refractive index as already mentioned in Section 2.1, is about $n = 1 - \delta \sim 1\text{-}10^{-5}$ for x-ray radiation, it will hardly be possible to prepare a lens or lens system for this range. This will be explained by an example. For a system made of refracting, curved surfaces we know:

$$\frac{1}{f} = \Gamma \cdot \sum_{i=1}^{n} \frac{1}{R_i}$$

And now to prepare a useful system, we need a large δ. Unfortunately, materials with large δ also absorb a lot of radiation, if we take for example, $\lambda = 0.71$ Å and use Beryllium as the refractive medium, then we obtain $\delta = 1.13 \cdot 10^{-6}$. Now if we equate R_i ($i = 1,n$) with 1 cm, the above equation shows that one would need 100 refractive surfaces in series in order to obtain f = 100 m ! In this case, almost no light intensity could penetrate. For these reasons, a lens system is impossible for the x-ray range.

Another possibility for an imaging system in the x-ray range is the Fresnel zone plate. In principle, it is a diffraction ring system with grid constant decreasing to the outside. The disadvantages of the zone plate compared to the Wolter telescope are considerable:

1. No efficiency
2. Higher image background due to passage of the 0-th diffraction order
3. Only small diameters can be manufactured
4. Large field of vision ↛ several zone plates ↛ adjusting problems.

The great advantage of the zone plate is due to the fact that spectroscopy can be operated simultaneously without any additional equipment because the focal length of the zone plate is dependent on wavelength. An additional advantage is the "ideal" imaging which is affected only by manufacturing tolerances.

Another imaging system in the x-ray range is the Baez telescope. /44
It consists of two perpendicular parabolic cylinder mirrors illuminated under oblique incidence. The advantage of this system over the Wolter Type I telescope lies in the significantly easier manufacture, the larger field of vision and large collector surfaces when using similar aperture dimensions for Baez and Wolter telescope. The disadvantage of this telescope is the inferior resolution which cannot be made better than 1 arcmin without considerable difficulty.

3. Fabrication of the 32 cm Wolter Telescope /45

The 32 cm telescope consists of four segments; two paraboloid segments and two hyperboloid segments. This design was selected for cost reasons since otherwise (one paraboloid, one hyperboloid) a separate polishing machine would have to have been built. In this case, we were able to use a modified turning lathe.

The material for the mirror dishes is a special aluminum alloy which was aged artifically in order to prevent changes in the telescope due to material deformations. First, the rough aluminum blank was lathed and drilled to its future shape on a NC turning lathe. The material stress was reduced by tempering. Next, minute working of the interior took place; depending on the mirror the surface was ground twice to a paraboloid or hyperboloid shape and subsequently lapped. Once this shape is obtained, the mirror was placed in an electrolytic nickel bath where it remained for several hours at a temperature of about 150° C. Kanigen is very hard and can therefore be easily polished to optimum quality. After this procedure, a Kanigen layer several 100 μ thick had deposited on the mirror. This layer was now polished and attention was paid to mating.

After polishing, the mirrors are moved to the x-ray test system of the MPE and are checked there for mating errors and scattering fraction. If there are deficiencies, they are returned to C. Zeiss Company in Oberkochen, where they are reworked. Inspection and reworking is repeated until the mirror corresponds to specifications. Then the four individual mirrors are provisionally mounted and adjusted. The telescope is fully illuminated and the mirrors are rotated and shifted to each other until the point image appears optimally in the microscope, whereby if possible, flaws in the individual mirrors are compensated against each other. Once this is satisfactory, the image is removed and processed by an analog secondary electron multiplier (called simply a SEV below).

The mirrors are then sent to Balzer Company where they are vapor /46
coated by an approximately 1,000 Å thick gold layer to increase the reflectivity. Final assembly, that is adjustment and screwing the individual mirrors together, is performed by C. Zeiss Company in Oberkochen. Finally, two plane-parallel glass plates are attached to the front and rear openings to seal the telescope and the interior of the telescope is filled with argon. The last working step, the assembly of two adjusting mirrors at the front aperture, is then performed by the MPE. As a final test, the entire telescope is checked again by the

X-Ray Test Center of the MPE.

4. Optical Tests on the 32 cm Wolter Telescope /47

The 32 cm telescope is tested twice in the optic spectral range: the first time by Zeiss Company before the individual mirrors are fitted together to form the telescope and the second time after the final approval by the MPE. Two different assemblies are used for this (see Figure 24,25).

4.1.1 Measurements at C. Zeiss Company (set up according to Figure 24)

In order to be able to fully illuminate the telescope, the image of a Xenon arch lamp was imaged by a lens in the shutter. The resulting divergent ray bundle is reflected by a mirror at 90° and falls on the parabolic mirror with a focal length of 3,785 mm which focuses it into a parallel bundle which impinges on the telescope. Behind the lens there is an interference filter for generating various wavelength bands. The image generated by the telescope can be observed either by the eye in a microscope or by means of a SEV with outlet connected electrometer and electronic page printer. The inlet opening to the SEV consists of a 30 μ perforated shutter. Observation takes place at the nominal focus, that is, 1,427.2 mm behind the bending point of the paraboloid-hyperboloid. The maximum resolution ability of the aperture was thus

$$\frac{\Delta x}{f} = \frac{3 \cdot 10^{-2}}{1427.2} = 4.3 \text{ arcsec.}$$

The available three wavelength bands were:

1. $\approx$ 2 540 Å $\pm \Delta\lambda$
2. $\approx$ 4 000 Å $\pm \Delta\lambda$
3. $\approx$ 7 700 Å $\pm \Delta\lambda$

The SEV was built onto a XYZ manipulator which could be moved along these three axes by means of stepping motor. At the beginning of measurements, the image was checked visually, then the SEV was run to the intensity maximum. We then moved it in the focal plane in a horizontal direction until no detectable intensity was found. From there, we moved in the opposite direction over the maximum down to the other side.

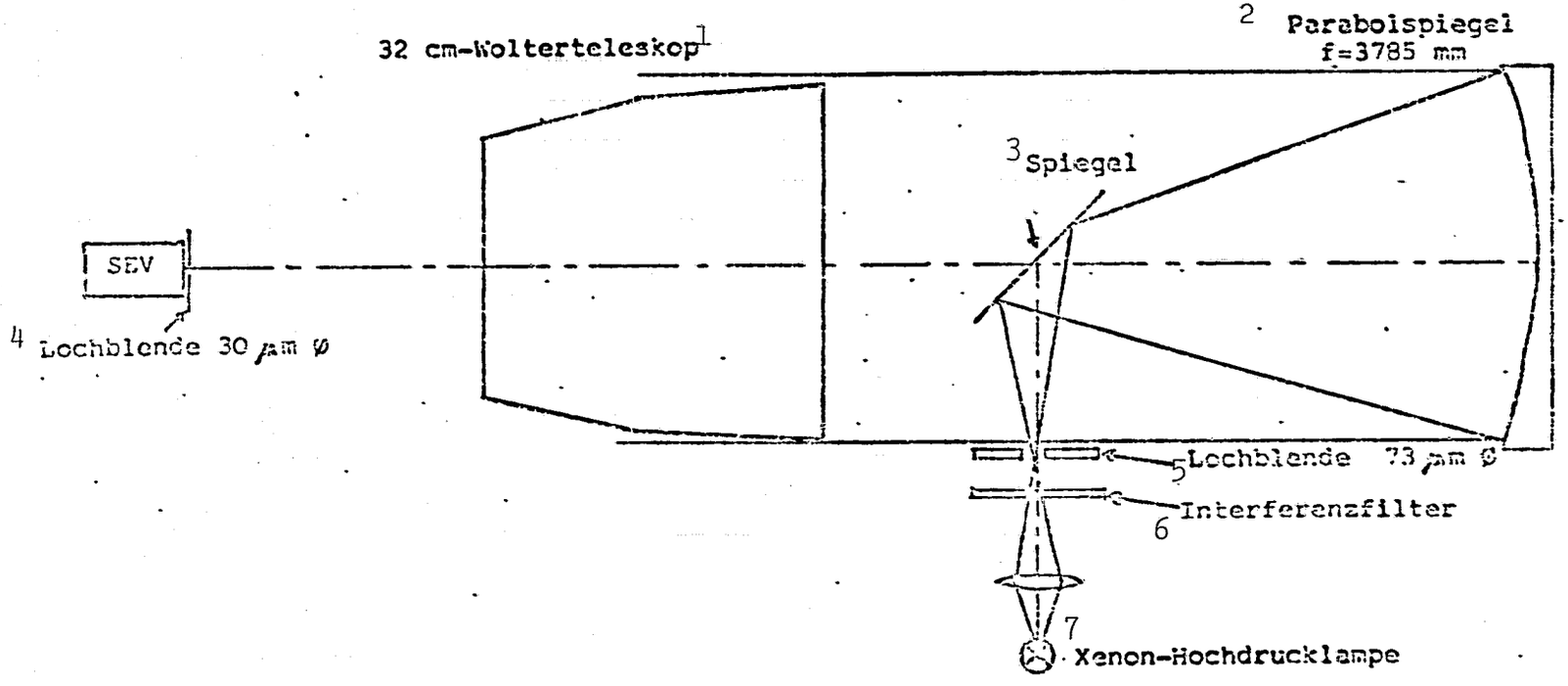

Figure 24: Optical measurement set-up for survey of the 32 cm Wolter telescope at C. Zeiss Company in Oberkochen (not drawn to scale)

Key: 1-32 cm Wolter Telescope 2-Parabolic Mirror 3-Miror 4-Perforated Shutter 5-Perforated Shutter 6- Interference Filter 7- Xenon High Pressure Lamp

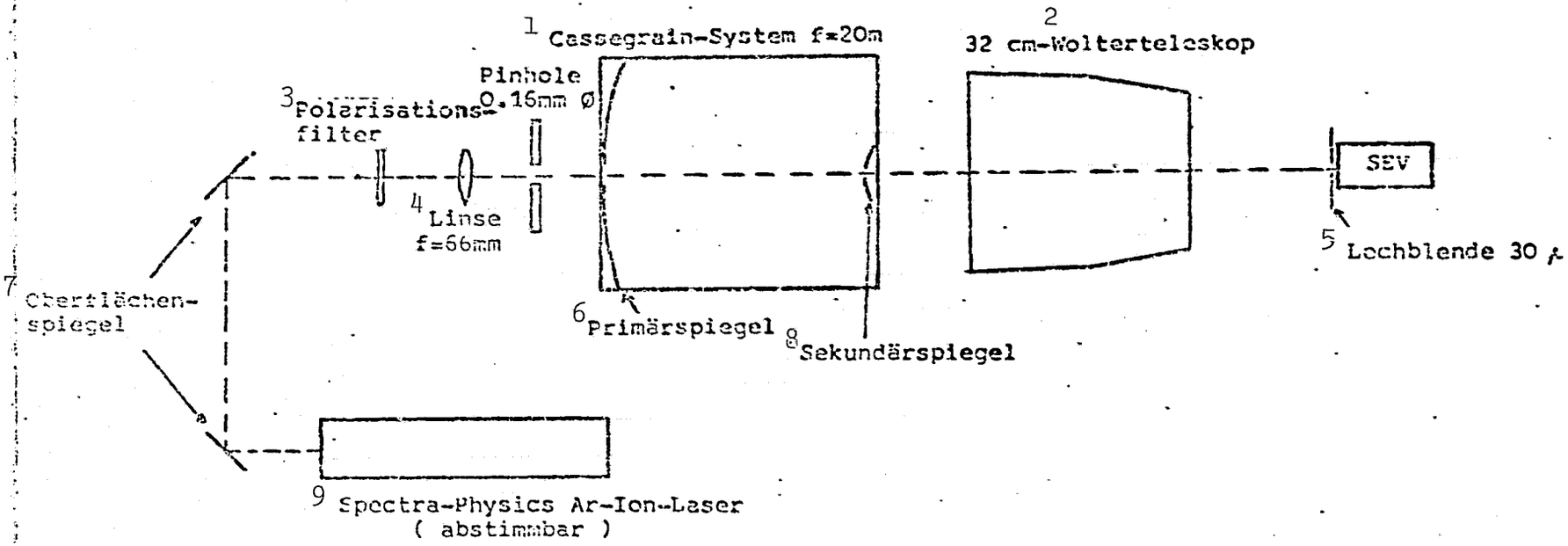

Figure 25: Schematic setup for optical tests on the 32 cm Wolter Telescope in Garching (hangar) (not drawn to scale)

Key: 1-Cassegrain System 2-32 cm Wolter Telescope 3-Polarization Filter 4-Lens 5-Perforated Shutters 6-Primary Mirrors 7-Surface Mirrors 8-Secondary Mirror 9-Spectra Physics Argon Ion Laser (adjustable)

4.1.2 Measurements at the MPE, Garching, (see Figure 25) /50

As a light source we had adjustable Ar-Ion-Laser which used three wavelengths: 4,545 Å, 4,880 Å, 5,145 Å. The beam was diverted twice by 90° with a collector lens (f = 66 mm) onto a perforated shutter of 160 µ diameter and expanded on a Cassegrain-System with f = 20 to ca. 40 cm diameter. We thus had a parallel light bundle of the named diameter. The 32 cm telescope was fully illuminated with this beam; the telescope itself was situated in a rotary mount about the vertical space axis. The image was recorded by C. Zeiss Company with a microscope or SEV and electronic system. Since the intensity of the laser was so high that the SEV was saturated, it was also necessary to add a polarization filter to attenuate the beam path. The SEV was operated with the same manipulator as was used by C. Zeiss Company. The measurement program consisted of seven measurements per y-shift, off-axis angle and wavelength. Here, the y-axis is the optic axis of the system. Including y = o (at the focus), five positions were measured (0, 0.4, 0.8, 1.5, 2.0 mm to the telescope) and for off axis angles (ε = 0, 10, 20, 30 arcmin). The scan took place in the x-direction, called the horizontal, and was run for seven Z-values (Z = -75, -50, -25, 0, +25, +75 µ). The rear shutter was mounted on the telescope to prevent rays which were reflected only by the hyperboloid from getting in to the SEV.

Figures 26 and 27 show typical profiles.

The following general requirements of such a setup must be met:

1. Homogeneous intensity over the entire surface of the incident beam (in order to be able to uniformly illuminate the telescope)

2. Accurate adjustment of the individual elements to the joint optic axis of the system (deviations $<$ 1 arcsec)

3. Sufficiently high intensity in order to be able to process a small pinhole or slit ($\varnothing$ $<$ 5 arcsec) for high resolution

4. Stability of the light source over longer periods of time (t $>$ 1h)

5. Non-vibrating assembly

6. Constance of scan speed

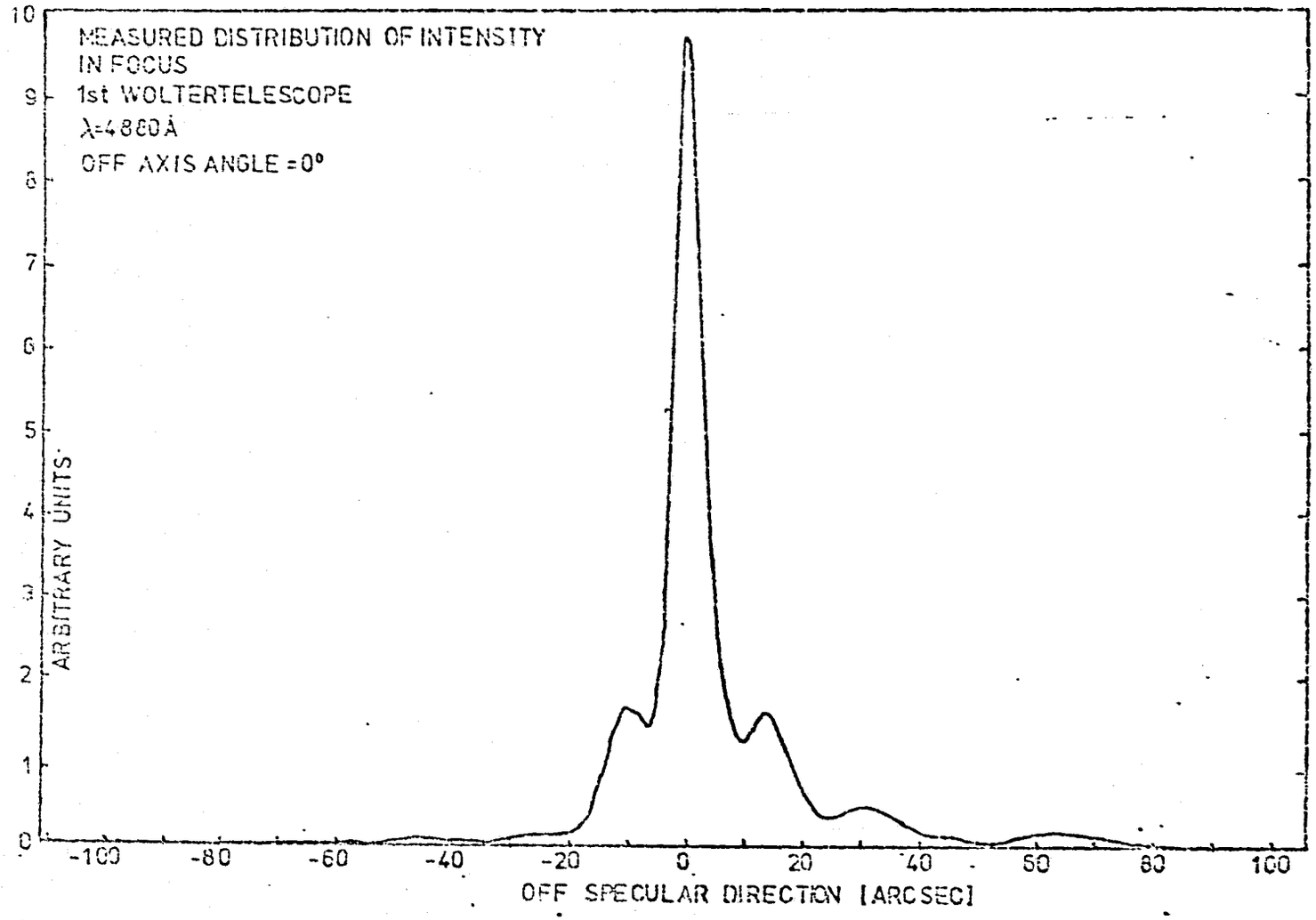

Figure 26: Measured intensity distribution in the focal plane of the 32 cm telescope (first telescope) at λ = 4,880 Å and $\varepsilon = 0^{\circ}0'\ 0''$

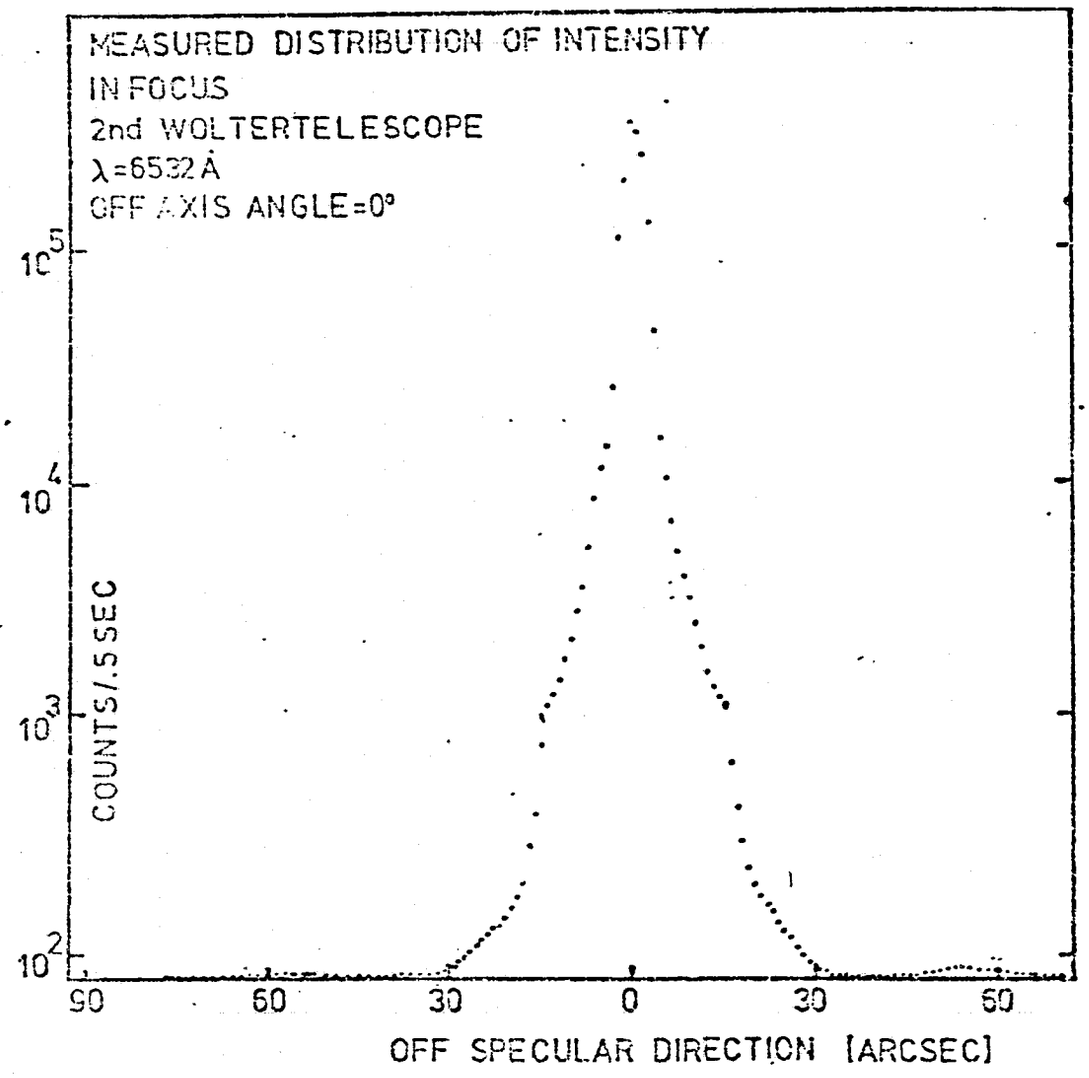

Figure 27: Measured intensity distribution in the focal plane of the 32 cm telescope (second telescope) at λ = 6 532 Å and $\varepsilon = 0^{o}\ 0'\ 0''$

4.2 Measured Results and Evaluation /53

Before presenting the measured results and their evaluation, several comments must be made on the apparatus and measurement itself.

In the course of measurement it turned out that is of extreme importance to illuminate the Cassegrain-System in an extremely clean manner (see Figure 25). This seems not to have been the case for a part of the measurements, but rather apparently, imaging of the diffusion figure of the pinhole took place. But it must be added, that a plane illumination is difficult to achieve since we have no actual criterion for establishing what actually is "good".

Another, even greater difficulty is hitting the focal plane and the center of the image with the 30 μ -Pinhole of the detector; this forms the starting point for all measurements. This objective was apparently not reached several times. At this point, we must point out the other potential for acquiring the image: the microscope. When observing the image in the telescope, naturally no quanitative statements can be made about it, however--this turned out in the course of measurements--quite reliable statements can be made about the quality of the image because it can be observed as a single whole. The statement of the experimentor, "the image is good now," is naturally dependent on his experience and attitude. However, this point does not seem to be too critical if we recall that the four segments of the 32 cm telescope were mounted by C. Zeiss Company using only light optic controls through the telescope for the entire mirror. At this point we should explain the assembly method: we begin with the two internal segments and turn and shift them until the image appears as an optimum in the telescope. Then the front paraboloid and rear hyperboloid are set on and these are again turned and shifted against the completed central piece until the image is again an optimum. This is very difficult since the front paraboloid and rear hyperboloid have to be optimally adjusted to each other, whereby simultaneously the focal point must lie in the middle piece. However, this method has the advantage that flaws in the individual segment (see Section 2.2) can be compensated by shifting.

But in order to make quantitative statements, a measurement /54
series was evaluated. The errors affecting these results can be estimated as 20% and they are due to the system itself. The results are compiled in the following table:

λ= 4 [illegible] Å			
Off Axis Winkel ε (arcmin)	Shift of Focal Plane (mm)	Point Image Width FWHM (arcsec)	Intensity at the Peak (%)
o	o	5.9	6o.7
o	o.4	6.9	76.3
o	o.8	6.4	65.4
o	1.5	1o.6	57.9
o	2.o	8.2	32.7
1o	o	8.9	24.5
1o	o.4	11.7	49.2
1o	o.8	11.7	3o.7
1o	1.5	6.3	53.7
1o	2.o	13.9	75.4
2o	o	9.1	79.3
2o	o.4	7.7	85.3
2o	o.8	6.3	81.3
2o	1.5	5.5	7o.3
2o	2.o	11.1	69.6
3o	o	1o.9	84.9
3o	o.4	11.9	74.5
3o	o.8	11.o	74.o
3o	1.5	7.1	81.8
3o	2.o	9.o	71.o

We can say the following: /55

1. The shift toward the telescope increases with increasing off axis angle in order to achieve optimum point image width

2. The intensities are generally too small in the peak .

Discussion of Point 1:

This result corresponds exactly to expectations (see Section 2.3). The reason that both times we found an optimum shift of 1.5 mm for 10 and 20 arcmin off axis, is most probably due to the large measurement error of 20% and also because only four measurement positions were used. For instance, at 10 arcmin, the optimum may actually have been 0.8 and 1.5 mm and at 20 arcmin, it may have been 1.2 and 2.0 mm. If this is correct, there is a constant increase in shift with increasing off axis angle, in accordance with the theory, for minimum blur circle radius. It also turns out that the required resolution of 20 arcsec was greatly exceeded. This certainly also confirms that it is correct to check the point image during assembly in the telescope and that one can make reliable, qualitative statements from an observation of the image.

Now we can go and check the resolution ability of the telescope if the fabrication-induced flaws from Section 2.2 were not present. Naturally, all mentioned flaws occur, but it is not known now large they are individually and how they interact. Therefore we shall investigate what would happen if the measured resolution of 5.9 arcsec FWHM were attributable to a single flaw. We will use the nomenclature from Section 2.2.

Flaw A5:

The deviation of the mantel line would be about 0.74 arcsec.

Flaw B2

The shift in axes against each other would have to be about 41 µ.

Discussion of Point 2:

If the profile looks like the example in Figure 25, then as a peak intensity we take everything inside the first two secondary minima on the left and right of the peak. Now as we see, a considerable fraction of the intensity lies outside these boundaries and this is due to the diffusion. In these cases, an imaging of the diffusion figure of the pinhole has taken place. Now if we add this diffused intensity as if it belonged to the peak, then the theoretical peak intensity of 95% is achieved everywhere (this intensity is given by the diffraction of the telescope, see Section 2.6). /56

5. X-Ray Measurements /57

5.1 Requirements of the Apparatus

Since x-ray radiation is absorbed by air, we are compelled to operate in a high vacuum. Since it is also practically impossible to generate an x-ray light bundle of large diameter and low divergence (angle < 30 arcsec), we must make use of a so-called pencil beam, a very thin bundle with a diameter of about 20 + 30 arcsec FWHM if we wish to realize paraxial incident radiation or a defined off axis angle.

The following requirements of the x-ray test system result:

1. The best possible vacuum ($p < 10^{-4}$ Torr)
2. Distance of the x-ray source from the target as large as possible
3. Potential for using different wavelengths
4. Stability of photon flux at the target ~ stability of the source and vacuum over long periods of time (t > several hours) important for measuring reflectivity
5. Smallest possible beam divergence
6. Fast, time and temperature-stable detection system
7. Stability of counter tube
8. Accurate alignment of source collimator, target and counting tube to the optic axis of the system
9. Manipulation of target and counting tube in all important directions (from the outside)
10. Inspection potential for all important quantities (emission flux, angle of incidence, position of target and counting tube).

5.2 The Apparatus /58

There is a "PANTER" x-ray test system at the institute and this meets the existing requirements; it was therefore used for the x-ray measurements (see Figures 28 and 30). It consists of a small vessel with an x-ray source flanged to one side and a 12 m long steel tube flanged to the other side. The other end of this tube opens into the target vessel (diameter: 2 m). On the opposite end of the vessel there is another tube containing the counter. The entire system is evacuated to a pressure of about 10^{-5} Torr by means of a rotary vane pump, turbo pumps and cryo pumps. There are two collimators (either pinhole or slit) located in the 12 m long beam tube*; these collimators provide a pencil beam of 23.9 arcsec FWHM in the target vessel when equipped with pinholes of 1.6 mm diameter. The source is about 15 m from the target and can be equipped with different anticathodes so that wavelengths of 5.6 + 44.8 Å can be generated. It is powered by stabilized voltage sources for heating and acceleration voltage, so that the fourth condition above is met. The photons are detected by a proportional counting tube containing $Ar\text{-}CH_4$ as counter gas. The pulses are recorded by the electronic system outlined in Figure 30. For all important quantities there is a possibility of measurement

* Translators note: Inconsistency in the original text

(vacuum, emission flux, etc.), in addition, the target can be moved from the outside in the x-direction, the counting tube can be moved in the x, y & z direction, the target can also be moved about the verticle space axis (z-axis) and the collimators can be moved in the x and z-direction by means of stepping motors. The entire system is aligned to one axis by means of a laser and a theodolite.

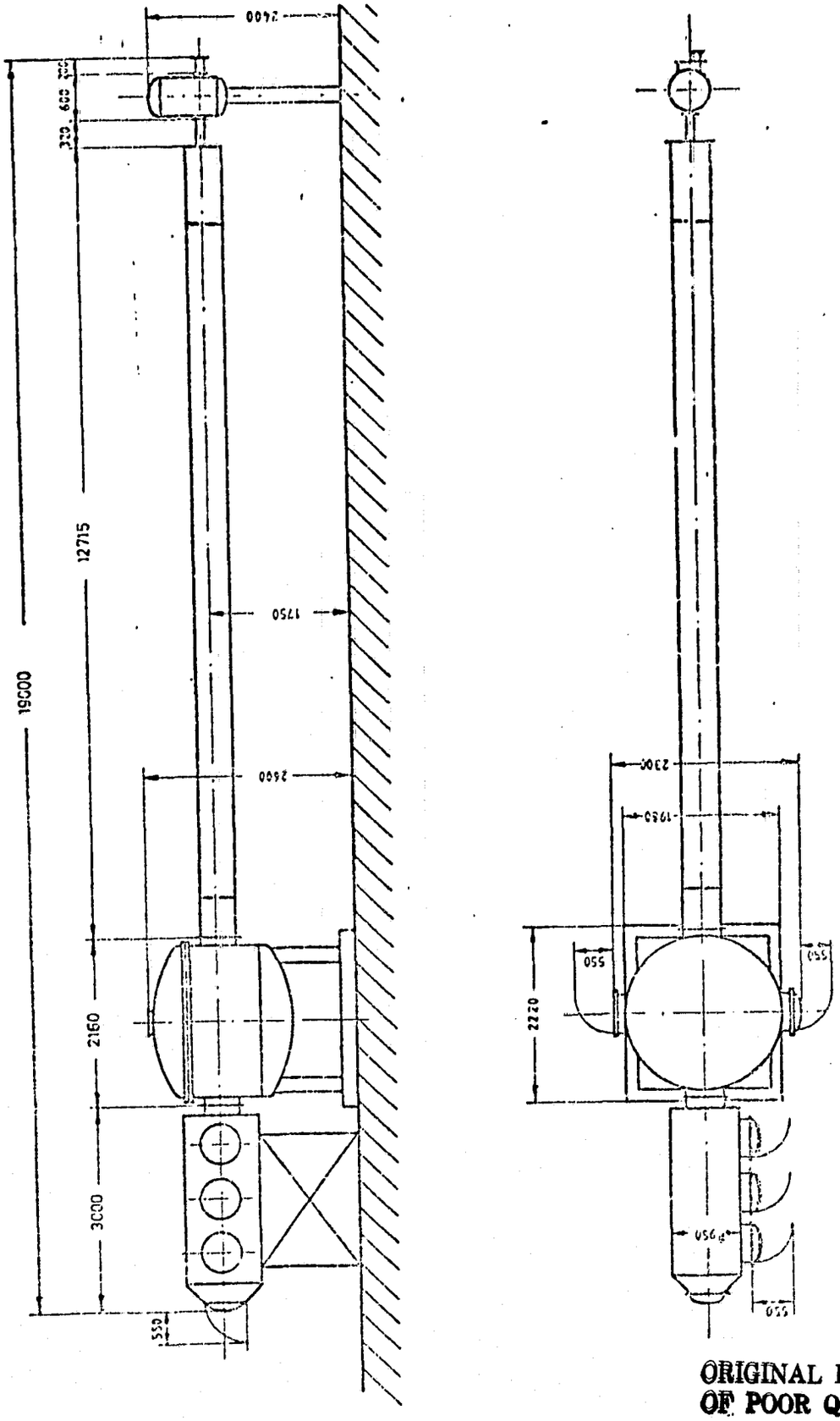

X-Ray Test facility "Panter"
MPE-Garching

Figure 28

ORIGINAL PAGE IS
OF POOR QUALITY

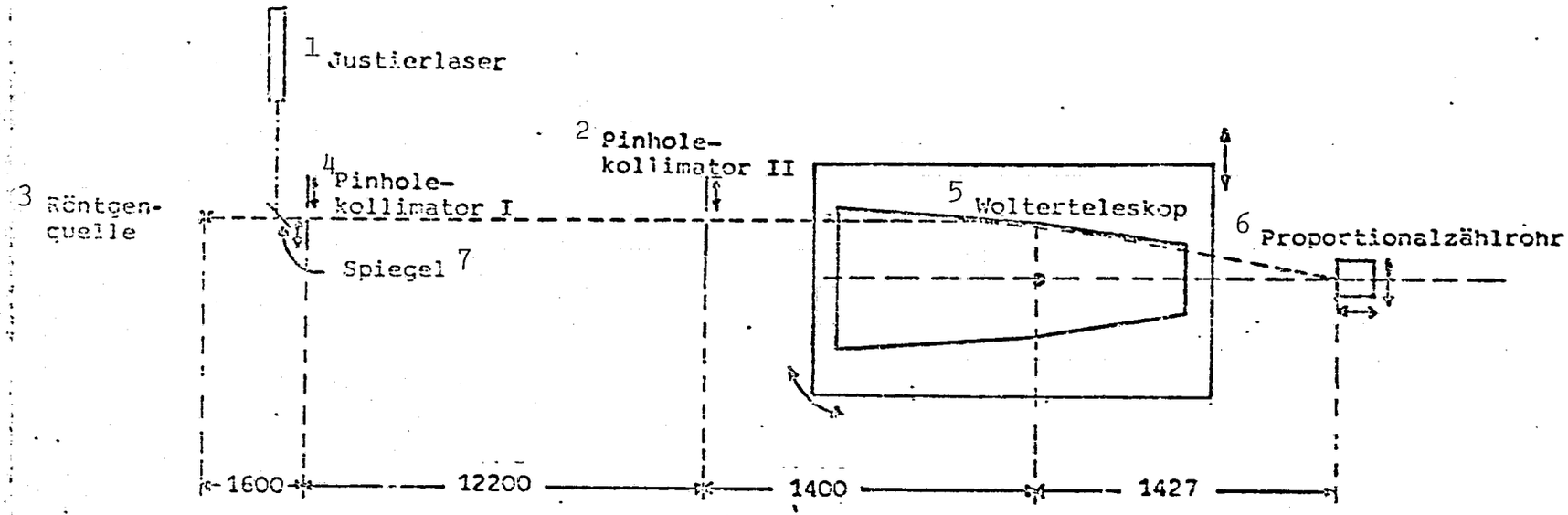

Figure 29: Schematic setup of the "PANTER" x-ray test facility

Key: 1- Adjusting Laser 2-Pinhole Collimator II 3-X-Ray Source 4- Pinhole Collimator I 5- Wolter Telescope 6-Proportional Counter Tube 7-Mirror

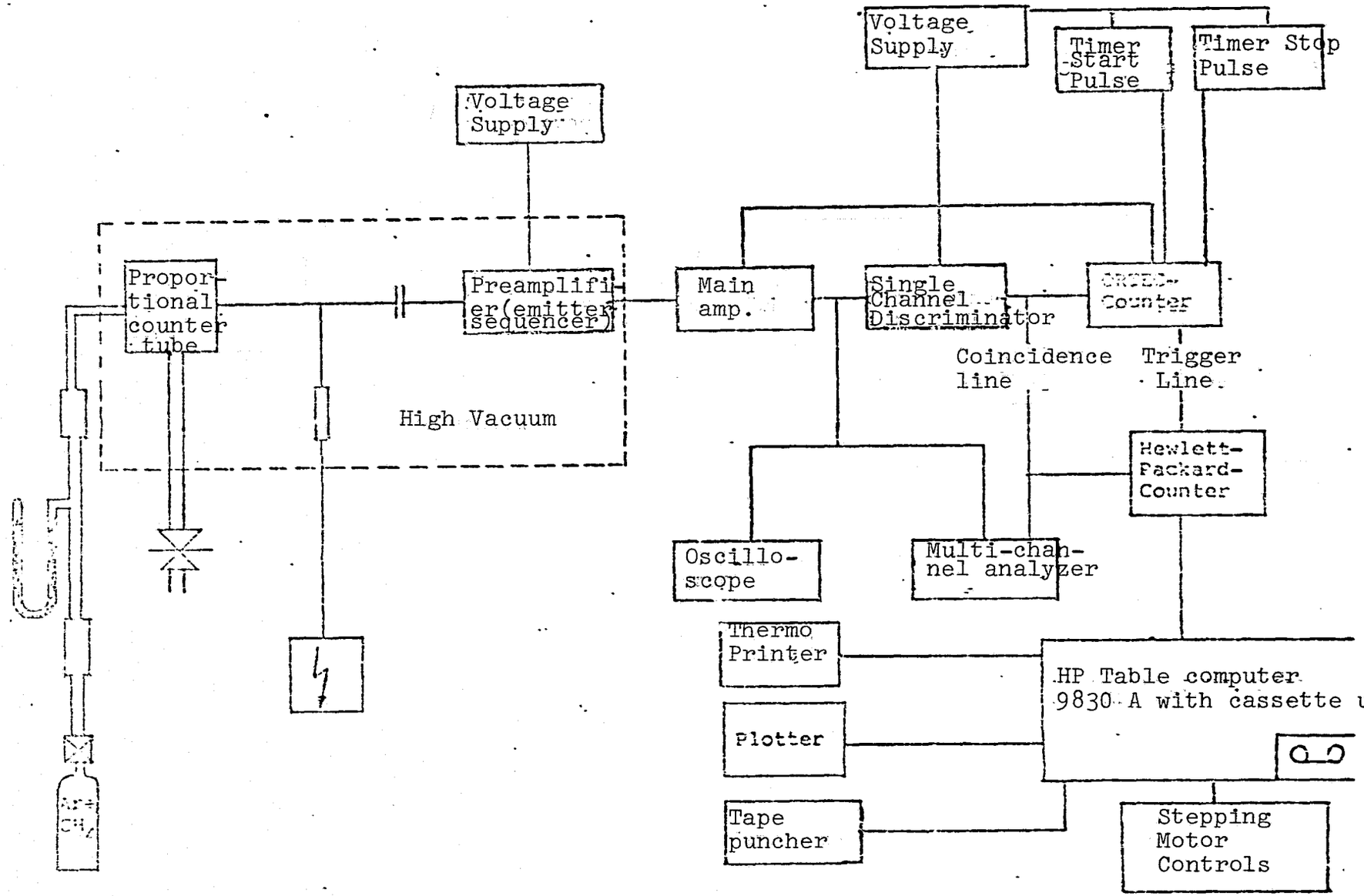

Figure 30: Block diagram of the "PANTER" electronic system

5.3 Performing the Measurements

/62

5.3.1 The Individual Mirrors

For implementation of the individual mirror measurements, a pencil beam of 23.9 arcsec FWHM was used exclusively in the Panter facility. The full width at the location of the counter tube was thus 2.7 mm and at the point of impact on the mirror, 2 mm (1.75 mm FWHM). The distance between point of impact and counter tube was 3200 mm. An entrance crevice of 300 μ was mounted at the counter tube. The paraboloids were aligned by a laser beam running through the optical axis of the system, to paraxial incident radiation and the hyperboloids were set to an angle of incidence of 1.5°. Using the counter tube, equal left and right horizontal movements from the maximum were run. As wavelengths we used $Al_{K\alpha}$ with 8.3 Å and $Cu_{L\alpha}$ with 13.3 Å, since only at these and shorter wavelengths is notable scattering expected and a check of microroughness by means of scattering was primarily the objective of the measurement. For the integration time, five seconds or ten seconds proved to be useful quantities. In addition, with each wavelength the direct ray was removed after the target had been moved from the beam path. Typical profiles are shown in Figures 31 and 36.

5.3.2 The Telescope Unit

The measurements on the finished telescope were performed in a manner similar to those individual mirror measurements. The same pencil beam was used. A 100 μ slit was used at the counter tube. The telescope was adjusted by means of a laser to paraxial incident radiation and the counter tube was set to the nominal focus. The scan again took place in the x-direction. One point on the first and second paraboloid section was measured for different azimuth angles and wavelengths. There were four wavelengths available $Al_{K\alpha}$ (8.3 Å), $Cu_{L\alpha}$ (13.3 Å), Fe (17.5 Å), $C_{K\alpha}$ (44.7 Å) Subsequently, the telescope was rotated about the z-axis in order to simulate off axis incident radiation. The counter tube was shifted in this case to the optic axis.

/63

5.4 Measurement Accuracy

As for all such measurements, the photon statistic plays an important role. If we count N photons, then the percentage error is given by

$$\frac{\sqrt{N}}{N} \cdot 100$$

Thus we can estimate that for our measurements near the peak, the error is about 2%, whereas in the wings of the scattering distribution it could amount to about 100% maximum, whenever the counting rate approximately corresponded to the background rate.

An additional source of error was the variation of photon flux during the measurement due to contamination of the source anticathode. This error can be estimated as about 5%.

For effeciency measurements, at the beginning and end of a measurement the direct beam was removed and then interpolated linearly over time between these two measured primary intensities. But this method was not always applied so that for instance, the individual mirror measurements are affected by the above error.

Another error was that we did not succeed in using purely monochromatic rays and the continuum fraction might have been about 5%.

In all, our measurement accuracy is estimated at about 10%.

5.5 The Measured Results /64

5.5.1 The Individual Mirrors

The individual mirror measurements were performed on the mirrors of the second 32 cm telescope. They do exhibit a similar scattering fraction, but a different angle distribution than the first telescope. A direct comparison of measurements of the individual mirrors and telescope unit is therefore not possible. Figure 31 shows the direct beam which was used for all measurements. Figures 32 and 36 show typical scatter distributions; the ordinate is distributed logarithmically, the abcissa is distributed linearly and both are given in minutes of arc. We can read off the following information:

1. The halo of scattering distribution decreases approximately according to a power law (e-function) at large scattering angles.

2. The altitude of the halo is dependent on wavelength as expected (large wavelength ⇝ lower halo).

3. The scattering distribution, altitude and shape, depend very much on the Kanigen and on the polishing.

4. Mating errors are not directly visible.

5. The reflectivity has its expected value within the error limits.

6. The peak width (FWHM) lies within the specification.

Discussion of Point 1:

What we can verify on the basis of figures or with our naked eye, namely that the scattering halo can be approximated by a straight line on a logarithmic scale, was also checked by calculation. For this, we evaluated equation 2.5.1 numerically. The profile of halo intensity is illustrated in Figures 32 and 36 by a solid line for the correlation length T which gave the optimum coordination. It turns out that the optimum correlation lengths always lie between 0.5 and 1.5 μ. Apparently, the average grain size of the polishing agent is reflected here. Deviations in the measured curves are caused either by photon statistics or by geometric shading effects during the measurement.

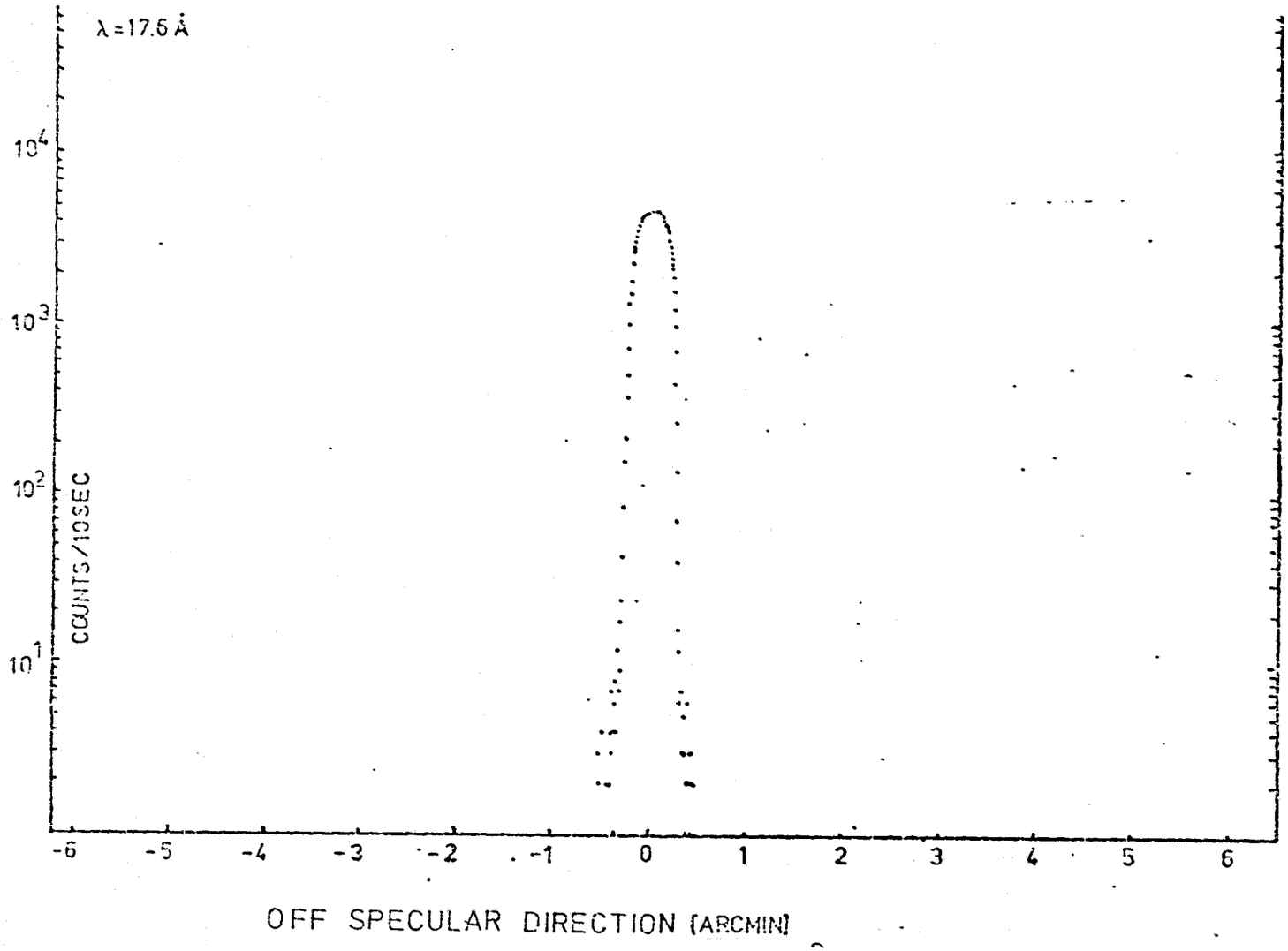

Figure 31: Measured profile of the direct ray at λ= 17.6 Å with the used collimators of 1.7 or 1.6 mm diameter (integration time: 10 seconds)

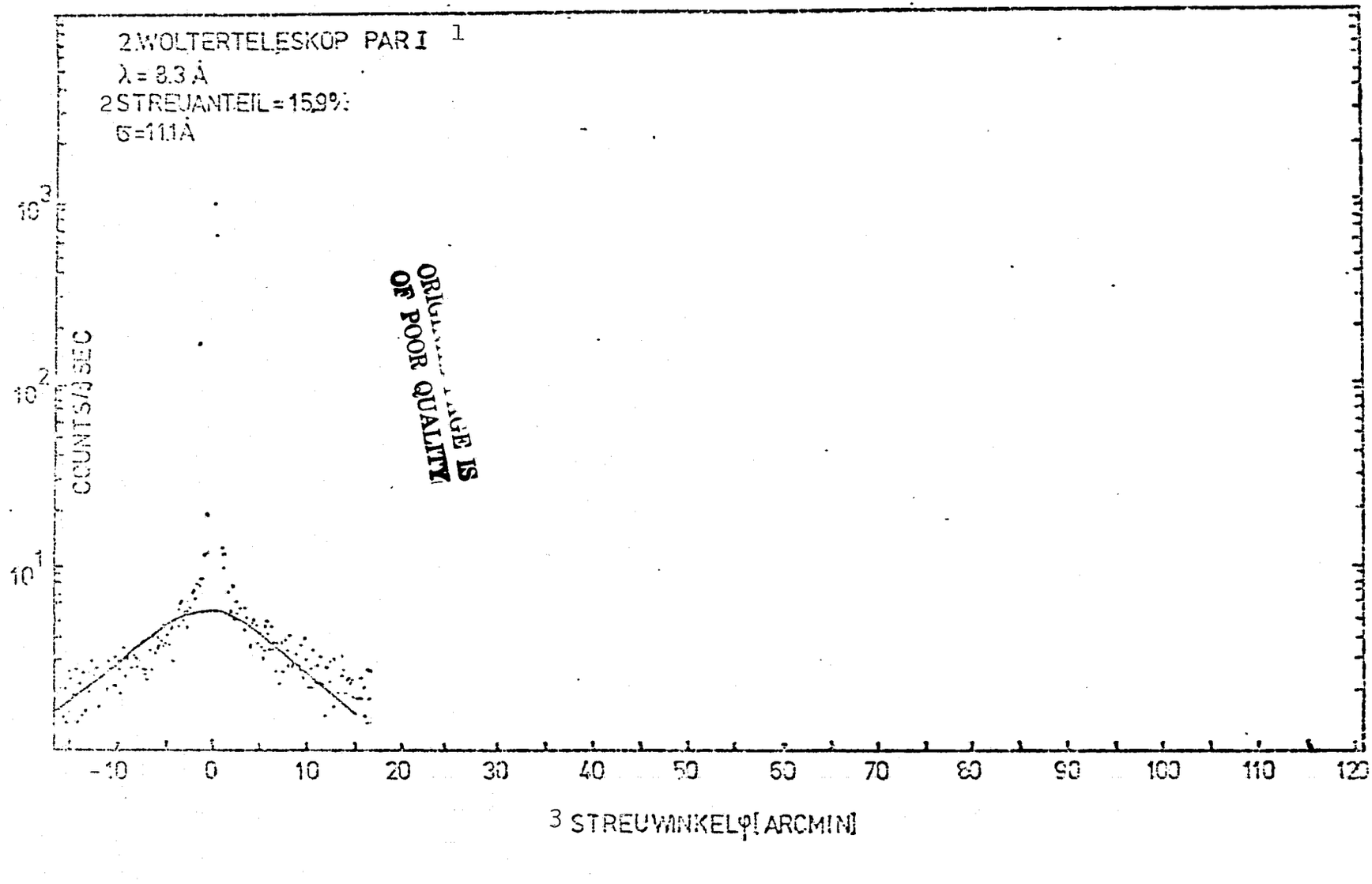

Figure 32: Measured scattering distribution at the front paraboloid of the second telescope at $\lambda = 8.3$ Å in polishing stage I (integration time: 9 seconds)

Key: 1- Second Wolter Telescope 2-Scattering Fraction 3-Scatteri ng Angle

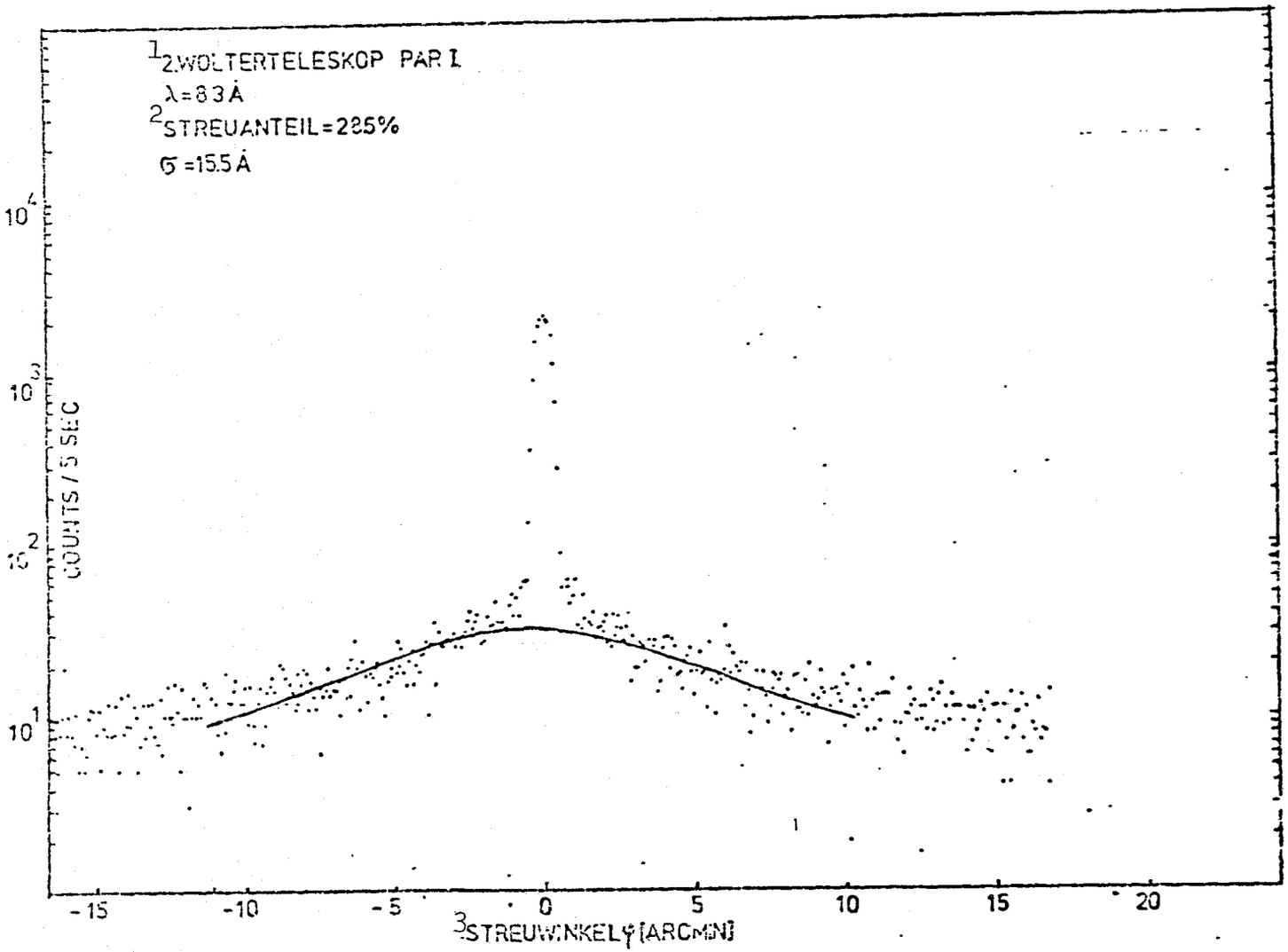

Figure 33: Measured scattering distribution at the front paraboloid of the second telescope at λ = 8.3 Å in polishing stage II (integration time: 5 seconds)

Key: 1- Second Wolter Telescope 2- Scattering Fraction 3- Scattering Angle

Figure 34: Measured scattering distribution at the front paraboloid of the second telescope at $\lambda = 8.3$ Å in polishing stage III (integration time: 5 seconds)

Key: 1-Second Wolter Telescope 2- Scattering Fraction 3-Scattering Angle

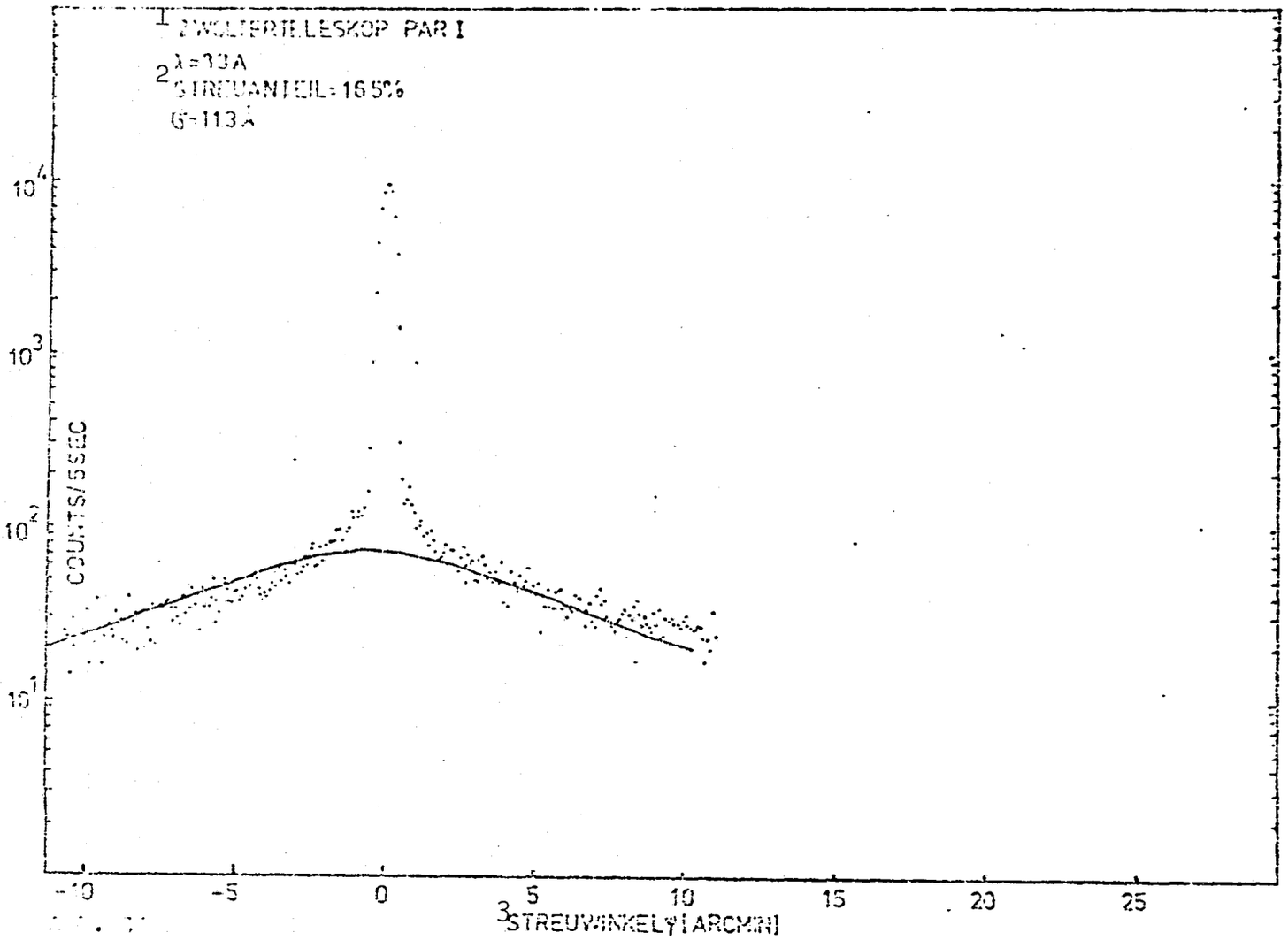

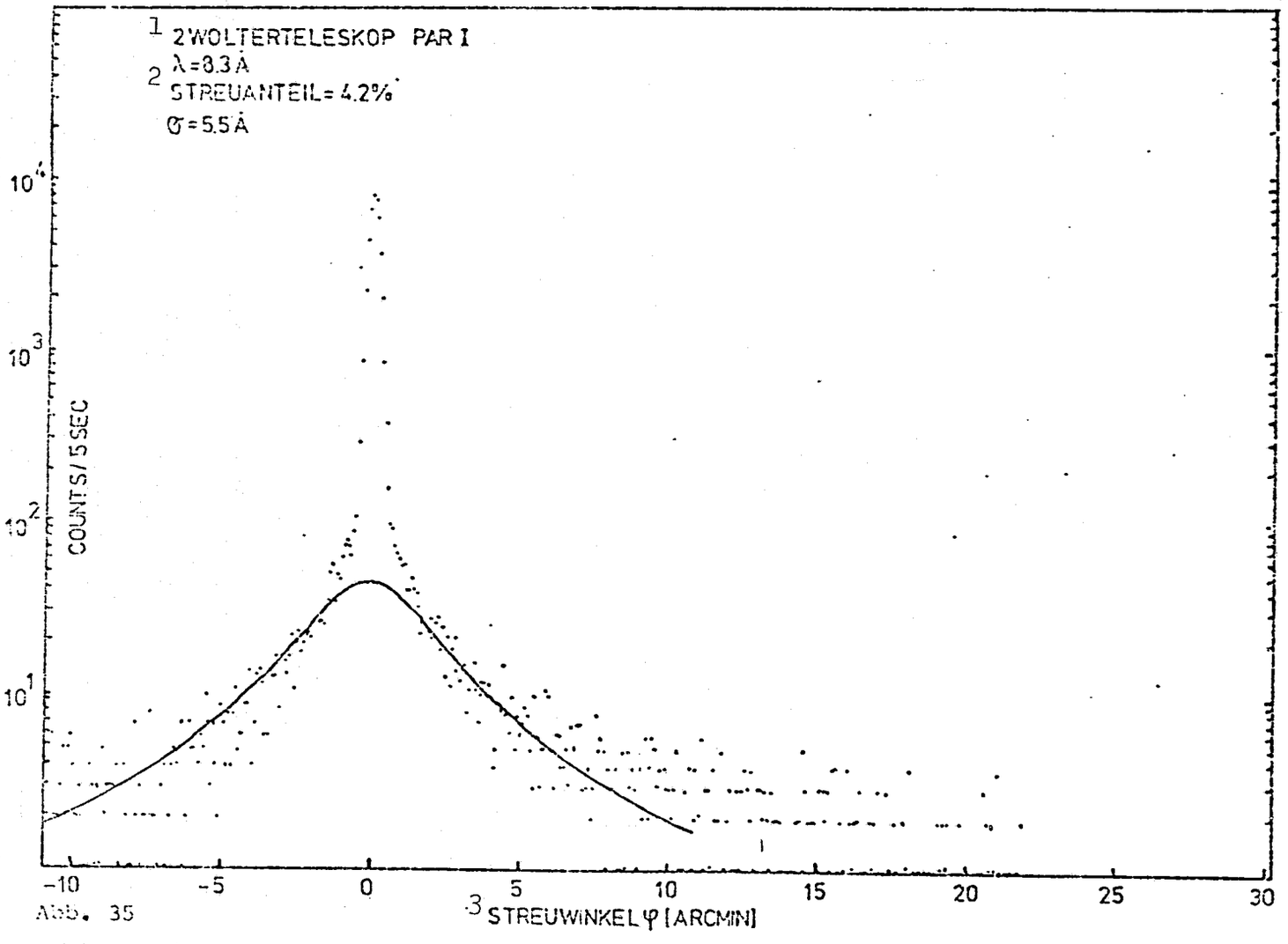

Figure 35: Measured scattering distribution at the front paraboloid of the second telescope at $\lambda = 8.3$ Å in polishing stage IV (integration time: 5 seconds)

Key: 1-Second Wolter Telescope 2- Scattering Fraction 3-Scattering Angle

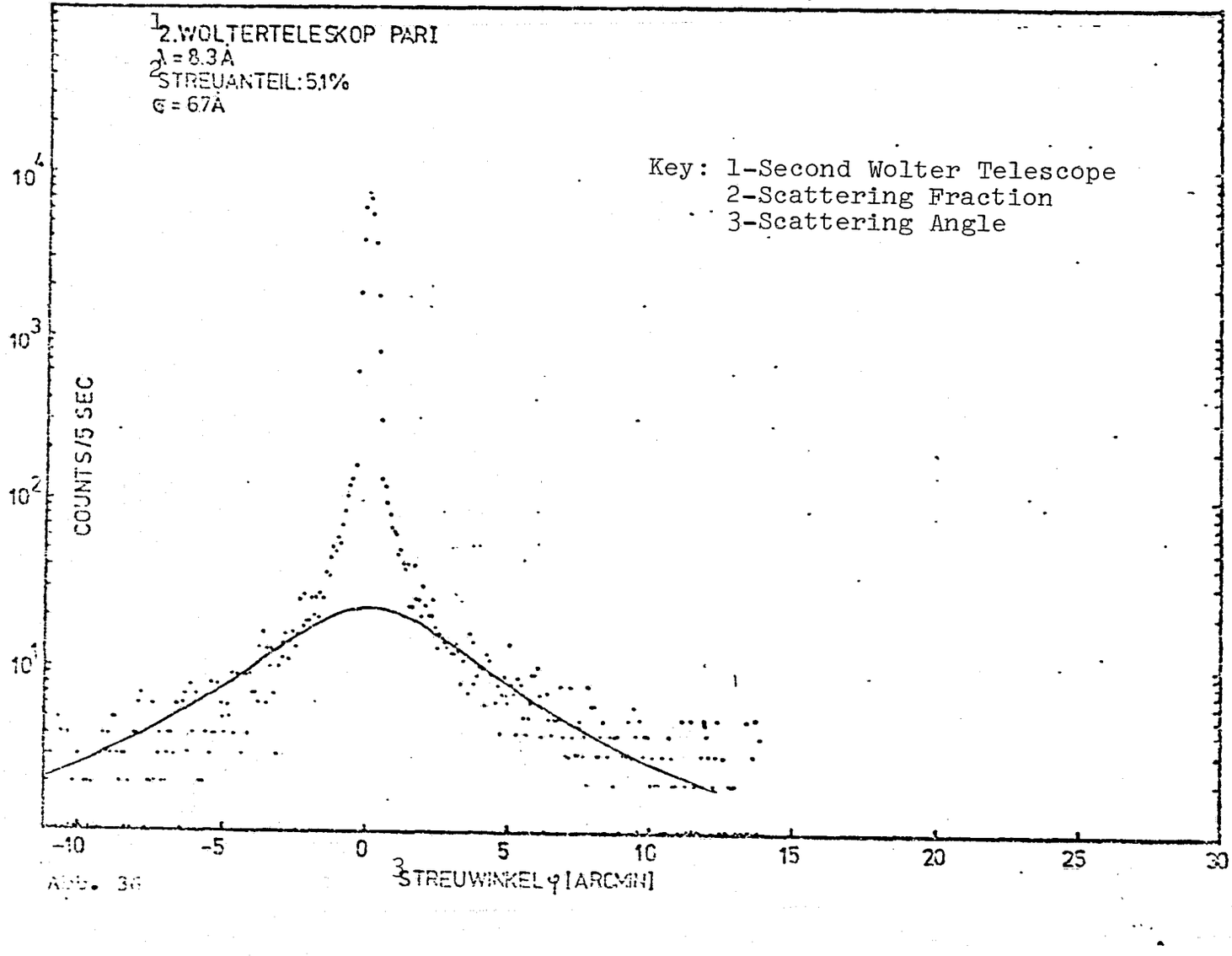

Figure 36: Measured scattering distribution at thefront paraboloid of the second telescope at $\lambda = 8.3$ Å in polishing stage V (integration time 5 seconds)

Discussion of Point 2:

The integral scattering fraction decreases according to equation 2.5.1 with increasing wavelength. This theoretical behavior was verified by experimental measurements within the error limits. The following table is presented:

TABLE 4: WAVELENGTH DEPENDENCE OF THE INTEGRAL SCATTERING FRACTION

λ(Å)	Scattering Fraction (%) exp.	Scattering Fraction (%) theor.	Mirror
8.3	16.5	-	Par 1
13.3	6.9	6.4	Par I
8.3	5.3	-	Par I
13.3	2.2	2.1	Par I
8.3	14.5	-	Par II
13.3	5.3	5.6	Par II

We proceeded from a measured scattering fraction at λ_1 = 8.3 Å and then according to $S(\lambda_2) = S(\lambda_1) \cdot (\frac{\lambda_1}{\lambda_2})^2$ for λ_2 = 13.3 Å, we calculated the scattering fraction and compared it to the measured scattering fraction $S(\lambda_2)$.

The measurements presented above were implemented on various mirrors (Par I and II) in various polishing stages. A comparison with 44.8 Å is impossible since the integral scattering fraction was in the range of the background in this case.

Discussion of Point 3:

Since the preparation of the studied Wolter telescope broke new technical ground both for the MPE as well as C. Zeiss Company, difficulties in fabrication occurred as expected. These were mainly due to surface quality, so that several polishing stages were needed to achieve the required scattering fraction. The production history of the mirror will be demonstrated on the basis of the front paraboloids serving to illustrate the process on all individual mirrors.

/72

Polishing Stage	Scattering Fraction (%)	Wavelength (A)
I	[illegible]	[illegible].3
II	23.4	[illegible].3
III	16.5	[illegible].3
IV	4.2	[illegible].3
V	5.1	[illegible].3

During the five polishing stages, C. Zeiss Company tested various polishing agents and even different grain size distribution. Thus, we can see the increase and decrease in the scattering fraction over the course of fabrication. Apparently, the quality of the Kanigen plays an important role. In the mirrors of the first telescope, it was probably greater than for those of the second, so that the scattering fraction could not be reduced below 4.2%. For the last polishing stage V, the scattering behavior worsened again slightly, however the fabrication had been terminated at this point in order not to grind through the Kanigan layer. Now if we compare Figures 33 and 34 with Figures 35 and 36, we see a definite difference in the shape of the scattering halo. Whereas the halo in Figures 33 and 34 decreases relatively uniformly at greater scattering angles, in Figures 35 and 36 we see that apparently small angle scattering is preferred. This can be explained by the change in grain size or grain size distribution of the particular polishing agent and this is also given in the FWHM of the scattering distribution, which becomes $\text{FWHM (rad)} = \frac{1}{T_{K\alpha}}$. Therefore, this is also expressed in the correlation length. The correlation length with which a good coordination can be achieved, lies at 1 μ in polishing stages I + III and at 1.5 μ in polishing stages IV and V.

Discussion of Point 5: /73

During the individual measurements, the direct ray (Figure 31) was measured, as already mentioned, in order to be able to determine the reflectivity. This lay between 53 and 60% which gives relatively good agreement with the theoretical value (20) of 62% at 8.3 Å for an error of 10%.

5.5.2 The Telescope Unit

Typical profiles are shown in Figures 35 and 42.

The scales are the same as those used for the individual mirrors. We can make the following determination:

1. The scattering agrees with the expected values (2 x S of the individual mirror).

2. Vapor coating of gold does not deteriorate the scattering behavior.

3. The FWHM of the peak is better than the specification.

4. Individual points exhibit mating flaws which may no longer be visible for total illumination.

5. The halo again has the approximate shape of a declining e-function.

6. The reflectivity agrees with the expected values.

7. The off axis behavior follows the theoretical considerations.

Discussion of Point 1:

According to Section 2.5, the integral scattering fraction should be twice as great as the simple reflection. This was demonstrated by experiment. As stated above, the measurements were performed on the individual mirrors of another telescope. But in the meantime, these mirrors were assembled into a telescope and surveyed. The scattering fraction was on the average $\lambda = .3$ Å at about 10% and for $\lambda = 13.3$ Å at about 5% within 20 arcmin diameter. Within the measurement accuracy, this gives a very nice agreement with theory. The other results again relate to the first telescope.

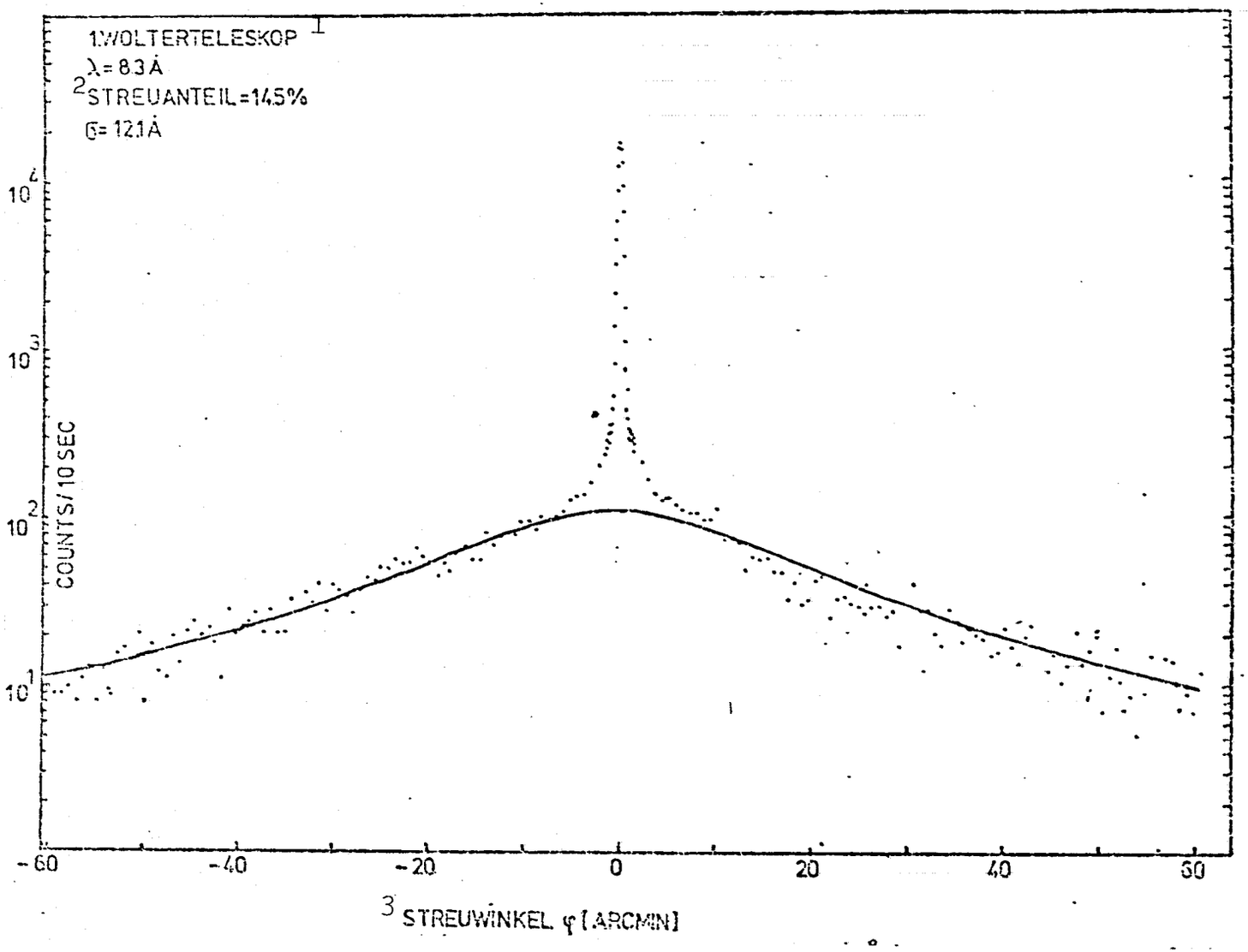

Figure 37: Measured scattering distribution on the first Wolter telescope at λ = 8.3 Å (integration time 10 ~~seconds), correlation length 1~~ μ

Key: 1-First Wolter Telescope 2- Scattering Fraction 3-Scattering Angle

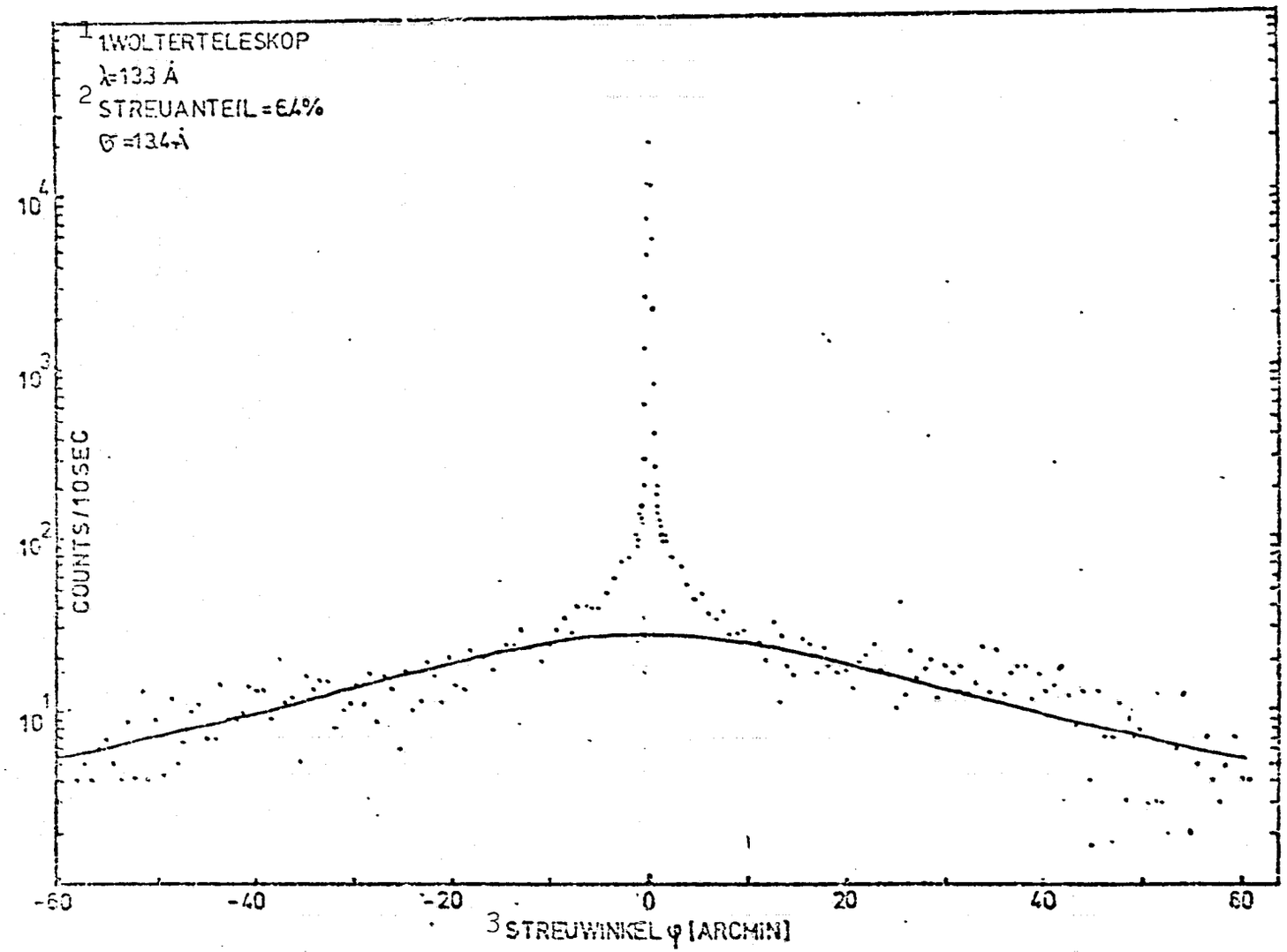

Figure 38: Measured scattering distribution on the first Wolter telescope at $\lambda = 13.3$ Å (integration time: 10 seconds), correlation length 1 µ

Key: 1- First Wolter Telescope 2- Scattering Fraction 3-Scattering Angle

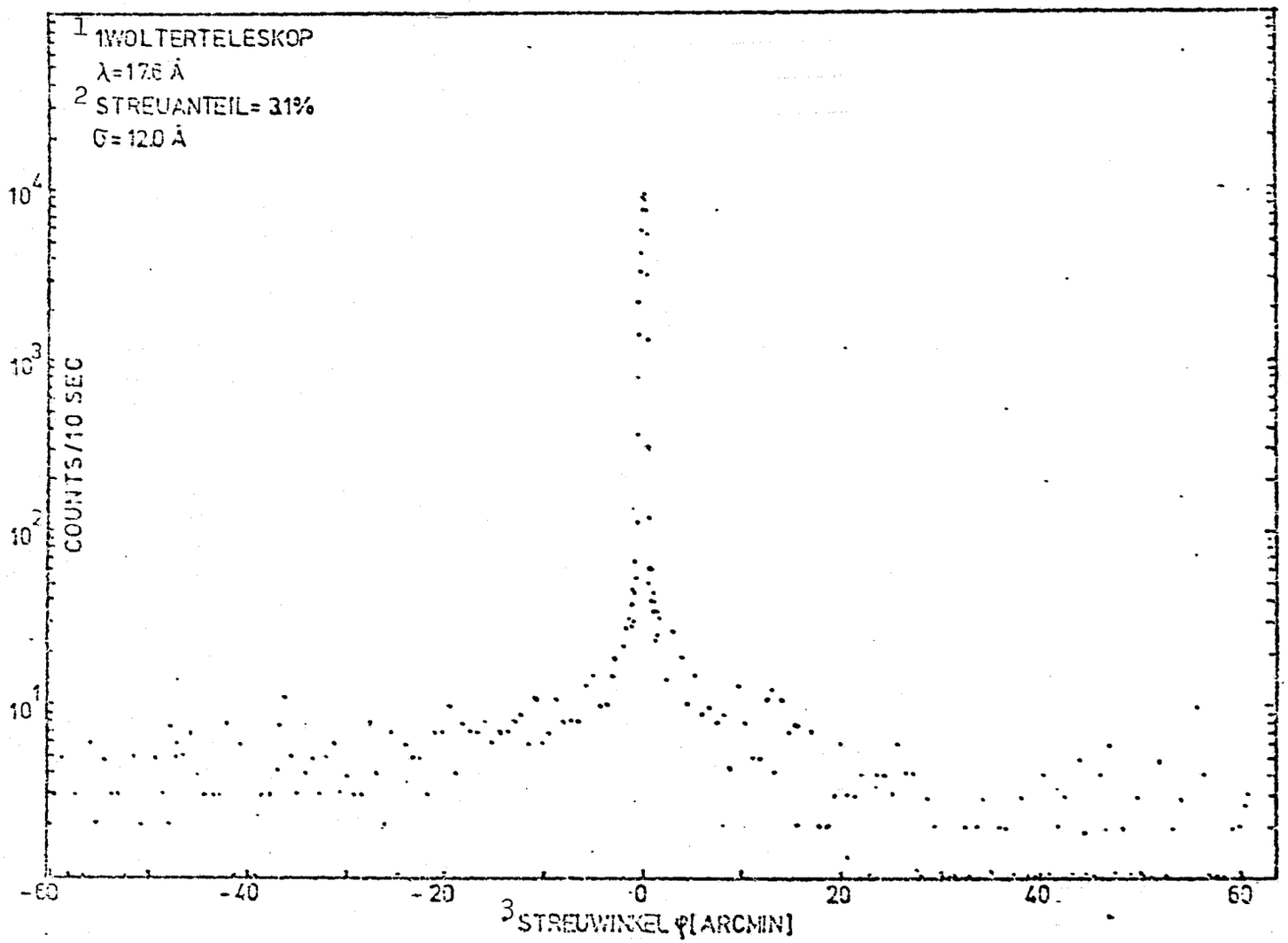

Figure 39: Measured scattering distribution on the first Wolter telescope at λ = 17.6 Å (integration time: 10 seconds)

Key: 1-Wolter Telescope 2-Scattering Fraction 3-Scattering Angle

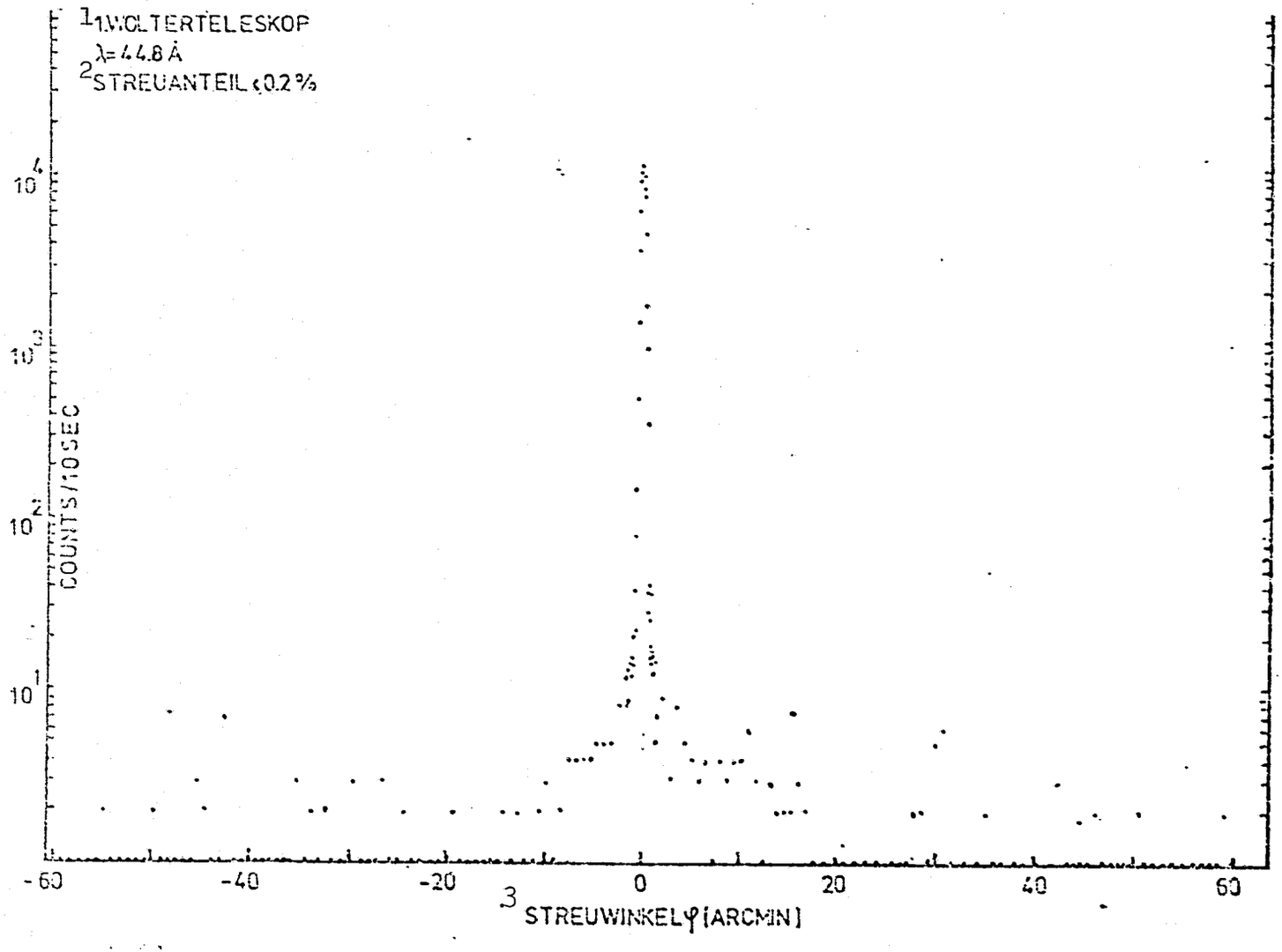

Figure 40: Measured scattering distribution on the first Wolter telescope for $\lambda = 44.8$ Å (integration time: 10 seconds)

Key: 1-First Wolter Telescope 2- Scattering Fraction 3-Scattering Angle

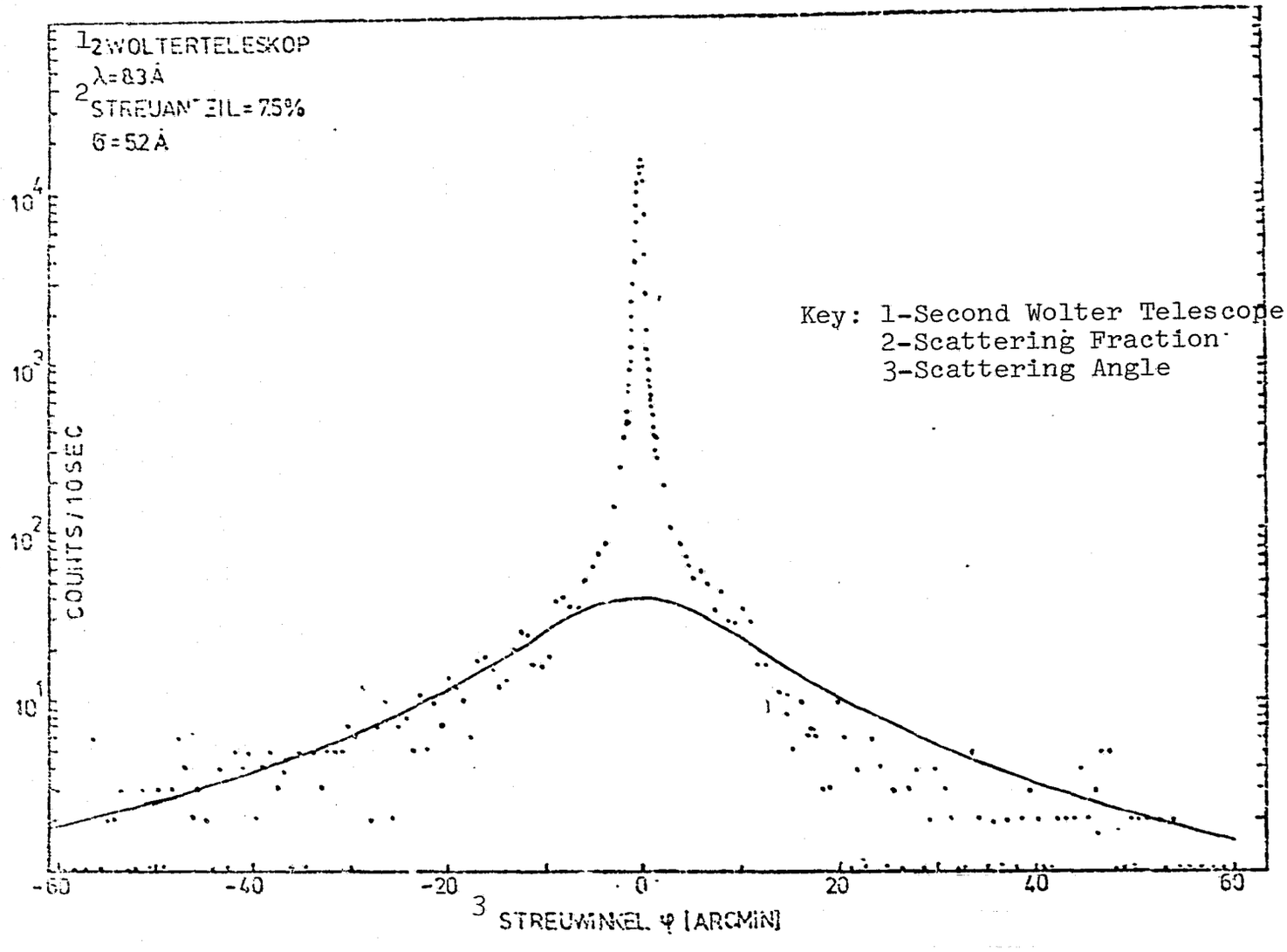

Figure 41: Measured scattering distribution of the second Wolter telescope at λ= 8.3 Å (integration time: 10 seconds); correlation length: /illegible

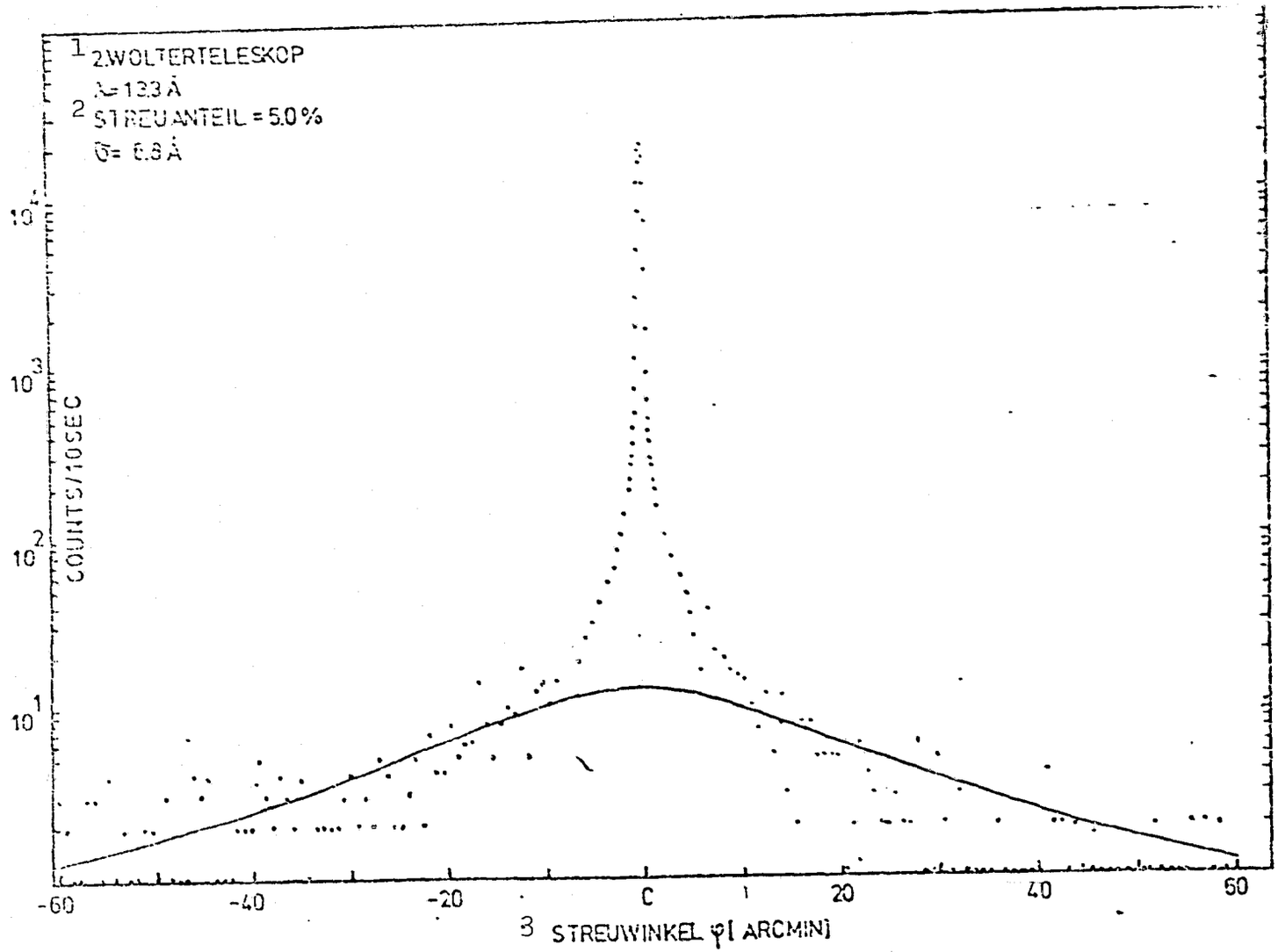

Figure 42: Measured scattering distributions on the second Wolter telescope at $\lambda = 13.3$ Å (integration time: 10 seconds), correlation length 1μ

Key: 1-Second Wolter Telescope 2-Scattering Fraction 3-Scattering Angle

Discussion of Point 2: /80

Whereas the measurements on the individual mirrors were taken with a Kanigen surface, the telescope unit was vapor coated with gold. Vapor coating of gold apparently does not affect the microroughness of the surface since otherwise, there would be no agreement in Section 1 and therefore the vapor coating must have been very homogeneous.

Discussion of Point 3:

From the number of measurements taken from the telescope, an average profile width of 25.3 arcsec FWHM results, so that if we add the amounts quadratically--which is certainly possible by close approximation--for the telescope and a collimator width of 22.9 arcsec FWHM and a counting tube crevice width of 9.0 arcsec FWHM, a width of 5.9 arcsec FWHM remains. This is in excellent agreement with the width measured in the optical range. At this point we mention again that the telescope was specified for 20 arcsec FWHM.

However, the small FWHM is not the only desirable factor, but it must also be assured that in the peak of the point image, the majority of the intensity will be found. With the 32 cm telescope, it happens that more than 85% of the energy is in the peak for $\lambda = 8.3$ Å. Another important point for the quality of such a telescope is the amplitude ratio of peak and scattering halo which determines the image contrast. With the present telescope the ratio for $\lambda = 8.3$ Å is better than 70. This is particularly important for its intended tasks (see Figures 37 and 42).

Discussion of Point 4:

The telescope was measured for various azimuth angles. At several places, slight "buckels" showed up on the flanks of the peak. These are attributable to mating errors of the meridian line. But since only individual points are affected, nothing more is seen of these flaws for full illumination. An estimation of the percentage of surface having tangent flaws greater than a certain value, is therefore impossible because the telescope, as mentioned, was measured only at a few points, and not integrally. The foregoing can also be confirmed by optical /81
measurements where no visible "buckle" was found in the profile.

Discussion of Point 5:

For the double reflection, the amount of the scattering fraction was greater than for single reflection, however the shape of the scattering profile must be retained. This was also confirmed (see Figures 36 and 41). A compensation line on a log scale was placed through the measurement point. In order to obtain a measure for the accuracy of mating, the so-called precision measure was calculated. This tells the probability of a measurement point lying on the e-function.

λ (Å)	Precision Measure
8.3	0.8[illegible]
13.3	0.73
17.6	0.73
44.8	0.12

The precision measure lies between 0 and 1. The probability that a point lies on the curve is 100% if it is 1 and 0% if it is 0. As we see from the above table, it is quite justified for 8.3 Å and 13.3 Å to place a e-function through the measurement point. Apparent difficulties occur if we also try to do this for 13.6 Å and 44.8 Å. But they are really only apparent difficulties if we consider Figures 39 and 40. For 17.6 Å and 44.8 A, the scattering halo is largely in the region of the dark counter rate, so that it is difficult to recognize a scattering halo here anyway. With these large wavelengths we would have to operate with significantly higher primary intensities in order to see a clear scattering halo. However, because of the finite dynamics of the proportional counter tube, this is not possible.

Now in order to see whether the simplifying assumptions with regard to scattering are also correct, calculations were performed with the same correlation length as used for the corresponding mirrors for the scattering halo of the second telescope unit (see Figures 41 and 42). The halo profile agrees quite well at the measured points so that the assumptions are considered justified. If we also apply this method to measurements at the first telescope, then we obtain correlation lengths of 1 μ. The reason for the different correlation lengths between the first and second telescope (1μ bzw. or 1.5 μ) is probably due to the different polishing agent which had to be changed from the first to the second telescope since the original polishing agent was no longer available. /82

Discussion of Point 6:

In his doctoral dissertation (14), R. Lenzen studied gold vapor-coated Karnigen surfaces and compared them to theoretical calculations. The basis of these calculations were values for the optical constants of gold which he took from B. Archenbach. Discrepancies occurred here which were also found during the measurements on the Wolter telescope; however, good agreement was achieved between our measurements and the Lenzen measurements. We present the following table on this:

TABLE 5: REFLECTIVITY

$R_{Aschenbach}$ (%)	R_{Lenzen} (%)	$R_{Woltertel.}$ (%)	λ(Å)
69	48	46.8	8.3
72	51	54.8	13.3
72	58	57.9	17.6
97	-	69.7	44.8

The given values were measured at 1.5° angle of incidence or were calculated at the same value. The values measured on the 32 cm telescope and the Lenz values cannot be compared directly since they were measured under the same conditions. To be sure, the Lenz values for the reflection coefficients come from measurements on flat mirrors, however there is no large difference between measurements on curved mirrors when the incident bundle is small enough (pencil beam).

The discrepancies to the Aschenbach values become understandable if we recall that they were calculated on a strict monochromatic basis, a condition which can never be realized in the experiment. In addition, in the course of measurements it turned out that the reflectivity always decreased with increasing scattering. This is a fact which has still not be explained.

Discussion of Point 7:

Since the telescope was measured only with a pencil beam, it could only be verified that the center of the point image came to lie at a deviation of $\varepsilon \cdot f$ (ε: off axis angle, f: focal length)/illegible/. It does not seem useful to make statements about the blur circle radius since for the existance of the scattering figure, a complete illumination of the telescope would be needed. In addition, for experimental reasons it was difficult (100 µ counter tube inlet slit), to determine the accurate focus of the telescope and corresponding shifts in the image plane and this is definitely necessary to check the off axis behavior (particularly/illegible/ blur circle radius). More accurate measurements are expected from a long-beam test (300 m distance) on a second Wolter telescope which can then be fully illuminated. In this regard, we refer again to Section 2.8 of this paper where it was mentioned that this is possible for a 300 m distance/illegible/ there, the off axis behavior including RMS blur circle radius should be detectable. These measurements however, were not yet concluded upon publication of this paper.

TABLE : COMPARISON OF THE EXISTING TELESCOPE WITH THE WOLTER TYPE I

	First 32 cm Telescope, 1 dish		Second 32 cm Telescope 1 dish		HEAO Telescope, 4 dishes		Exosat Prototype, 1 dish	
Largest Diameter (cm)	32		32		58		27.8	
Geometric Collector Surface	1o6.o42		1o6.o42		~5oo		52.7	
	Spec.	Measurement	Spec.	Measurement	Spec.	Measurement	Spec.	Measurement
FWHM (arcsec) Optic	20	5.8	20	4.9				21
X-Ray	20	5.9	20		2	3.5	10	23
Effective Service Area (cm^2) at 0.93 KeV	27.6	31.8	27.6	35.3		~200	18.7	14.9
Scattering Fraction (%) at 0.98 KeV in 26 arcmin Ø	2 ÷ 8	6	2 ÷ 8	3		~7	3	16
Roughness G (Å)		12		6.8	< 30	24÷29	~30	

Comparison With Other Wolter Type I Telescopes /85

In conclusion, a comparison of the 32 cm telescope with the Exosat and the HEAO-B telescope is permitted. In all fairness it must be said that the Exosat telescope is a prototype and that the final telescope will probably be better. Both the HEAO-B as well as Exosat are instruments for use on satellites.

If we examine Table 6, we see that the 32 cm telescope diameter is closer to the Exosat but that the other data are more comparable to the HEAO-B. The smaller collector surface of 52.7 cm^2 for the Exosat is due to a smaller angle of incidence and smaller mirror length. The high resolution of 3.5 arcsec for HEAO-B is surprising, however, it must be noted that this was one of the main requirements during fabrication. In comparison to this, the 32 cm telescope with 5.9 or 4.9 arcsec FWHM is still quite good if we consider that it was specified only for 20 arcsec. Since with the HEAO-B, the specification of 2 arcsec was not reached, that indicates the enormous difficulty of such a project, particularly the severe problems with four-fold clustering and the inherent weight of the mirror which alone is enough to distort it. A comparison with Exosat should be done with care because it is a prototype. Nevertheless, with 23 arcsec it is quite above the pack, the same is true for the scattering. It is greater than HEAO-B by a factor of two and better than the first 32 cm telescope by a factor of 2.6. If we calculate the scattering fraction of HEAO-B to the same angle of incidence as the 32 cm telescope then we arrive at about 40%. Therefore, it is probably entirely justified to designate the 6% or 3% of the 32 cm telescope as good performance since metal surfaces can never be polished as well as glass. The microroughness of 24 and 28 Å for HEAO-B can probably not be correct. Both due to measurements within the framework of this paper as well as due to measurements by R. Lenzen, the scattering theory presented here is confirmed. If we use this as a basis for a scattering fraction of 8% at 0.93 KeV, then according to Figure 1 we arrive at a roughness of about / illegible /.

In conclusion we can say that HEAO-B is presently the best x-ray telescope, both with regard to efficiency as well resolution. However, we must not forget the care that had to be taken in its preparation. But the 32 cm telescope is also quite good, particularly under consideration of the fact that it was a "initial product" of the MPE and C. Zeiss Company. With regard to Exosat it remains to be seen how this telescope will develop. /86

7. Outlook

A Wolter Type I telescope with a maximum diameter of 80 cm is currently in the planning stages at the institute; it should be ready for use by 1980. Unlike the 32 cm telescope with metal reflector, it will have a glass-ceramic mixture. In this case, the difficulty with the 32 cm telescope, like porosity of the surface, difficulties in polishing and assembly of the four segments are not expected. It consists only of one parabolic and one hyperbolic section. From initial measurements on material samples we can already conclude that the surface will cause fewer problems.

With this telescope, which will consist of four dishes, we will have a very powerful instrument with which we will be able to discover 10,000e new x-ray sources in the heavens.

8. Summary /87

From the MPE, a contract was issued to C. Zeiss Company, Oberkochen for the preparation of three Wolter type I telescopes with an opening of 32 cm and a focal length of 1,427.2 mm measured from the bending paraboloid-hyperboloid point. They were specified for a resolution ability of less than 20 arcsec and a scattering of less than 12% at a wavelength of 8.3 Å. Within this dissertation, the properties of the 32 cm telescope were studied. Measurements on the individual mirrors composing the telescope as well as measurements on the assembled telescope both in the optic and x-ray range form a part of this. From the optic measurements, no information was expected on the scattering behavior since at about 5000 Å the integral scattering fraction makes up only fractions of a percent. However, the resolution ability of the first telescope was determined as 5.9 arcsec FWHM and the off axis behavior was perfected according to the theory. Optical measurements were also made during fabrication of the telescope in order to optimize the point image. This is probably the greatest importance of these measurements.

Due to x-ray measurements on the individual mirrors, the microroughness and thus the scattering behavior were checked during fabrication. Severe difficulties both with the Kanigen coating (porosity) as well as selection of polishing material showed up. Sometimes up to five polishing stages were needed to meet the requirements of the scientific mission (observation of astrophysical scattering halo). At the same time, the mirrors were checked for mating errors and reflectivity. No practical difficulties occurred here.

The x-ray measurements on the first finished telescope were used practically as a final test before flight in order to learn the imaging properties of this mirror and to see whether the gold vapor coating had deteriorated the mirror (scattering). The latter question can be answered in the negative. The imaging properties in all cases follow the theoretical values in measurement accuracy (scattering, reflectivity, off axis behavior).

Better and more reliable information can only be made for the second telescope which will be subjected to a long-beam test on a 300 m range of the Marshall Space Flight Center after the conclusion of this work. /88

9. Literature

(1) M. Born & E.Wolf, Principles of Optics, 1959 /89

(2) W. Werner, in Applied Optics/Vol. 16, No3/march 1977

(3) J.D. Mangus & J.H. Underwood, in Applied Optics/ Vol. 8, Nol/January 1969

(4) L.P. VanSpeybroech u. R.C. Chase, in Applied Optics/ Vol. 11, No2/February 1972

(5) H. Wolter, in Annalen der Physik, No. 6, V. 10, 1952, p. 94 ff.

(6) M.A. Blochin, Physik der Rontgenstrahlen, /Physics of X-Ray Radiation/ VEB Verlag Technik, Berlin, 1957

(7) P. Beckmann & A. Spizzichino, The Scattering of Electromagnetic Waves from Rough Surfaces, Pergamon Press, 1963

(8) H. HeBberg, schriftl. Mittellung, 11-26-76, 3-14-77

(9) Hubert F.A. Tschunko, in Applied Optics/Vol. 13, No8/August 1974

(10) G.C. Steward, in Cambridge Tracts in Mathematics and Mathematical Physics, No25, Cambridge University Press, 1928

(11) B.L. Mehta, in Applied Optics/Vol. 13, No4/ April 1974

(12) Hubert F.A. Tschunko, in Applied Optics/Vol. 13, Nol/January 1974

(13) H. Wolter, in Annalen der Physik, No. 6, V. 10, 1952 p. 286 ff.

(14) R. Lenzen, Doctoral Dissertation, MPE, 1978

(15) P. deKorte, Exosat Private Communique, 7-5-75

(16) J. Eastman & P. Baumeister, The Microstructure of Polished Optical Surfaces, Opt. Comm., Vol 12, No4, p. 418 (1974)

(17) M. Born, Optik /Optics/ 3rd ed., Springer, Berlin 1972

(18) P. Kirkpatrick & A.V. Baez, in Journal of The Optical Society of America, Vol. 38, no9, 1948

(19) G. Mollenstedt, H.J. Einichammer, K.H.v. Grote, U. Mayer, "Some Current Problems in X-Ray Optics", in X-Ray Optics And Microanalysis, September 1965

(20) T. Zehnpfennis, R. Giacconi, P. Hasserty, W. Reidy, G. Vaiana, A Laboratory Program To Develop Improved Gracing Incidence X-Ray Optics, NASA Tract, Washington, February 1967

I wish to thank Professors Dr. K. Pinkau and Dr. J. Trumper for the opportunity of performing this doctoral dissertation at the Max-Planck-Institut for extra-terrestrial physics in Garching.

My special gratitude is due Dr. H. Breuninger for his tremendous support and intensive management during the work.

I also wish to thank the Physicists M. Harle, P, Predehl and R. Lenzen for a number of valuable hints, tips and conversations and last but not least, my fiance Britta who with great effort deciphered my script and typed the manuscript.